

October 2020

Analysis of Computational Modeling Methods as Applied to Single-Crystal Organohalide Perovskites

Jon M. Bebeau

University of South Florida

Follow this and additional works at: <https://digitalcommons.usf.edu/etd>

 Part of the [Electrical and Computer Engineering Commons](#)

Scholar Commons Citation

Bebeau, Jon M., "Analysis of Computational Modeling Methods as Applied to Single-Crystal Organohalide Perovskites" (2020). *USF Tampa Graduate Theses and Dissertations*.
<https://digitalcommons.usf.edu/etd/9526>

This Thesis is brought to you for free and open access by the USF Graduate Theses and Dissertations at Digital Commons @ University of South Florida. It has been accepted for inclusion in USF Tampa Graduate Theses and Dissertations by an authorized administrator of Digital Commons @ University of South Florida. For more information, please contact scholarcommons@usf.edu.

Analysis of Computational Modeling Methods as Applied to Single-Crystal
Organohalide Perovskites

by

Jon M. Bebeau

A thesis submitted in partial fulfillment
of the requirements for the degree of
Master of Science in Electrical Engineering
Department of Electrical Engineering
College of Engineering
University of South Florida

Major Professor: Arash Takshi, Ph.D.
Rudy Schlaf, Ph.D.
E. K. Stefanakos, Ph.D.

Date of Approval:
October 24, 2020

Keywords: Methylammonium Lead Iodine, Computational Molecular Dynamics, Inverse
Temperature Crystallization (ITC), Computational Chemistry

Copyright © 2020, Jon M. Bebeau

Dedication

I wish to thank my wonderful wife, Muriel, for her support and encouragement throughout this effort. The time and attention needed to research this thesis and document findings significantly impacted our life plans, yet unwaveringly, Muriel supported my study. Thank you dear.

I thank my major professor, Dr. Arash Takshi, for his guidance and support throughout this protracted academic adventure, down many a blind alley and a crooked mile, to be politely and professionally nudged back onto the straight and narrow. On the many occasions when all seemed lost, a calm discussion would clear the fog and offer inspiration. Thank you Dr. Takshi.

Table of Contents

List of Tables	iii
List of Figures	iv
Abstract	vi
Chapter 1: Introduction	1
1.1 Methylammonium Lead Halide Perovskite Structure	2
1.2 Motivation for This Research	4
1.3 The Origin and History of Perovskite Development.....	7
1.3.1 Perovskites Photovoltaic Applications.....	12
Chapter 2: Computational Material Science Methods	15
2.1 Background of Existing Methods.....	15
2.2 Force Field Molecular Model.....	16
2.3 Schrödinger Equation	18
2.4 Born–Oppenheimer Approximation.....	20
2.5 Hartree Electron Position Approximation	22
2.6 Hartree-Fock Equation	23
2.7 Hartree-Fock and Linear Combination of Atomic Orbitals.....	25
2.8 Density Functional Theory.....	26
2.9 Generalized Gradient and Hybrid Approximations	29
2.10 Planewave Pseudopotentials	30
Chapter 3: Computational Methods Results	34
3.1 Force Field Optimized Model	35
3.1.1 The Unit Cell.....	39
3.1.2 Selection of the Supercell	40
3.2 DFT Ground-State Calculations and Results.....	41
3.2.1 Exact Exchange (HF) Hybrid PBE0	42
3.2.2 PAW Projector Augmented Waves w/SOC.....	43
3.2.3 Generalized-gradient Approximation Model.....	44
3.2.4 Ultrasoft (Vanderbilt) Pseudo-potentials	45
3.3 Summary of Methods Results	46

Chapter 4: Conclusions	49
4.1 Future Research	50
References	51
Appendix A: Copyright Permissions	57
Appendix B: NREL Best Research-Cell Efficiencies as of 08/03/2020.....	59

List of Tables

Table 1	Pseudopotential libraries	32
Table 2	Modeling optimizations final structure result summary	48
Table 3	Published band gap values by others.....	48

List of Figures

Figure 1.1	Typical structure of MAPbI ₃	4
Figure 1.2	(A) 2D layer of model perovskite octahedra.....	4
Figure 1.3	Single-crystal growth in solution	5
Figure 1.4	Sample MABr ₃ single crystal of 5mm grown by ITC.....	5
Figure 1.5	Early publication on lead halide perovskites	8
Figure 1.6	Publication in Nature, Wells, H.	10
Figure 1.7	Image from Kojima, A., 214th ESC Meeting, Abstract #27 Paper	11
Figure 1.8	Perovskites inset of NREL Best Research-Cell Efficiencies as of 08/03/2020.....	13
Figure 2.1	Pseudopotential and pseudo-wavefunction comparison.....	33
Figure 3.1a	Orthorhombic MAPbI ₃ created atom by atom with MA cation omitted.....	36
Figure 3.1b	Orthorhombic MAPbI ₃ without polygons	36
Figure 3.2	MA cation showing dipole moment and axis reference.....	38
Figure 3.3a	Orthorhombic MAPbI ₃ created atom by atom with polygons.....	38
Figure 3.3b	Orthorhombic MAPbI ₃ without polygons	38
Figure 3.4	Unit cell outlined in thin black reference line, with polygons.....	39
Figure 3.5	Unit cell with bonded atoms outside the Unit Cell, without polygons	39
Figure 3.6a	Super cell “top” view <1,1,0>	41
Figure 3.6b	Super cell “front” view <1,0,0>	41

Figure 3.7a	Exact exchange (HF) hybrid PBE0 band structure.....	42
Figure 3.7b	Exact exchange (HF) hybrid PBE0 band DOS	42
Figure 3.8a	PAW with spin orbital coupling band structure.....	43
Figure 3.8b	PAW with spin orbital coupling DOS.....	43
Figure 3.9a	GGA corrected band structure.....	45
Figure 3.9b	GGA corrected DOS.....	45
Figure 3.10a	Ultrasoft pseudo-potentials band structure.....	46
Figure 3.10b	Ultrasoft pseudo-potentials DOS.....	46
Figure B.1	NREL Best Research-Cell Efficiencies as of 08/03/2020	59
Figure B.1a	Perovskites inset of NREL Best Research-Cell Efficiencies as of 08/03/2020.....	59

Abstract

Perovskite, specifically MAPbI₃, has exploded onto the electronic material forefront, with applications from photovoltaic to optical sensors. Still, there remain many unanswered questions about the electronic, structural and mechanical processes and properties of this perovskite. Computational software exists to model the electronic structure and material properties, to the nano scale, using density-functional theory. The goal of these models is to parallel the physical science of the substance in a computer simulation based on emerging mathematical models of the quantum mechanical behavior.

In this study I review the historical use of perovskites in electronics, review the evolution of DFT algorithm developments and select four of the popular DFT algorithms to model and analyze the behavior of MAIPb₃ to compute the energy structure, volume, density, band gap and density of states of a supercell. Two methods are determined to generate plausible but faulty results due to offsetting errors. The computed results are compared with published results from others. The need to incorporate spin-orbital coupling modeling is identified. The results for this research provide foundation for future research to explore application of computation materials modeling for electronic material development.

Chapter 1: Introduction

Hybrid organic-inorganic perovskites are the subject of much research due to their application in photovoltaic. Still, these electronic materials are finding other applications in an emerging field.

Metal-halide perovskites have been studied for their semiconductor properties since the 1950's [2]. Recently, organic-inorganic perovskites such as $\text{CH}_3\text{NH}_3\text{PbI}_3$, methylammonium lead iodide (MAPI3), have been recognized for their application in solar cells. Noteworthy is that perovskites with an organic group coupled with an inorganic crystal frame have been found to be excellent photo absorbers.

Remarkably high photoconversion efficiencies are realized for a solution-based process near ambient conditions. While much research effort continues improving the solar conversion efficiencies, perovskites see other applications as electronic materials in light emitting diodes [3], thermoelectric [4], low-light optical sensors [5] and solid-state memory devices [6].

Research continues into the physical and electronic properties of perovskite material, with a wealth of reported findings characterizing the physical and optical properties [7, 8], band structure [9, 10], geometry [11], absorption spectrum [12] and chemical stability [13, 14]. Yet, many facets of this unusual substance remain unclear or garner conflicting reports. The nature and type of hydrogen bonding, along with other noncovalent interactions in this elastic metallic-cage restraining the methylammonium free cation, and the role and effects of this methylammonium molecule remain unclear [15, 16]. The processes responsible in the

hysteresis of the material are speculative [17-19]. The processes of polarization reported in the tetrahedral phase near room temperature [19, 20], the piezo effect [21], the significant discrepancies between measured and calculated bandgap energy reduction [22], the origins of reported tilting of the Pb-I matrix in the tetrahedral phase and even the type of the crystallographic space group are confusing and open for clarification [23]. It is believed that all open questions are related to the molecular and crystalline structure dynamics of the material and are the focus of this thesis. A detailed simulation study of the material can provide good explanations to some of the observed properties.

1.1 Methylammonium Lead Halide Perovskite Structure

Hybrid perovskites are well-known minerals of the type ABX_3 stoichiometry, form a crystal with the organic A cation localized within an inorganic frame BX_3 of a corner sharing octahedra. Common cation A site include methylammonium (MA), $CH_3NH_3^+$ and formamidinium (FA), $CH_2N_2H_4$. Species of halide on the X site include Cl^- , Br^- and I^- . Metal at the B site include Pb^{2+} and Sn^{2+} . Substitution of the metallic and inorganic elements lead to diverse physical and chemical properties [24, 25]. The $CH_3NH_3PbI_3$ (MAPbI₃), the focus of this study, illustrated in Figure 1.1 [26], a common depiction of MAPbI₃, so common that Wikipedia “Perovskite (structure)” references this image. It is composed of a PbI_6 framework corner sharing octahedra and a single methylammonium, $CH_3NH_3^+$ cation occupies the center A site which is enclosed by 12 neighboring iodine ions corner-sharing the PbI_6 octahedra. The methylammonium cation, is not covalently bound to the Pb-I frame and is free to roam within the forcefield constrained and influenced by the Pb-I frame and adjacent methylammonium cations. Each of the PbI_6 octahedra consists of a lead atom, hidden by the green tetrahedral shaped visual adornment

between 3 adjacent iodine atoms shown in purple. This framework of interconnecting Pb-I atoms, extending in 3 axes with sharing corner iodine atoms, exist throughout the crystal. While the depiction in Figure 1 is chemically accurate, the representation is misleading in the illustrated geometry. The illustration visually indicating the geometry of the Pb-I framework is uniform with right angles between iodine atoms and the Pb atom is centered within the iodide tetrahedrons. Other researchers propose the octahedral structures are tilted from the 2D rectangular image Figure 1.2 (A) to that of Figure 1.2 (B) [1]. The cause and effects of tilting on the electronic properties of MAPbI₃ is profound and complex with several proposed explanations [12, 21, 27, 28]. Further, Lee et al. [28] conducted a research study at ground state ignoring the temperature effects of the electronic material at usable temperatures.

Research groups have studied the perovskite structure using single-crystal neutron diffraction, nuclear magnetic resonance and X-ray diffraction methods to study the structure of the basic particles [29-34]. Published findings confirm the atomic structure, but only to some extent [30, 35-40]. Due to the relatively large size and electronic complexity of lead and along with the presence of the slightly smaller iodide, accurate measurements of the location and orientation of the methylammonium molecule is difficult and any information regarding the hydrogen bonding is well beyond current instrumentation.

This computational analysis will focus on methylammonium lead iodide, CH₃NH₃PbI₃ (MAPbI₃) as this species is widely used in commercial application with a significant body of published experimental data for reference.

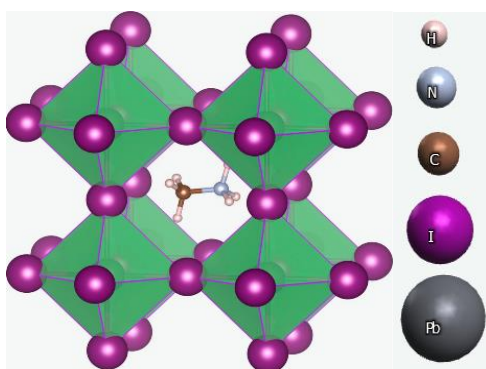


Figure 1.1 Typical structure of MAPbI₃ [25]

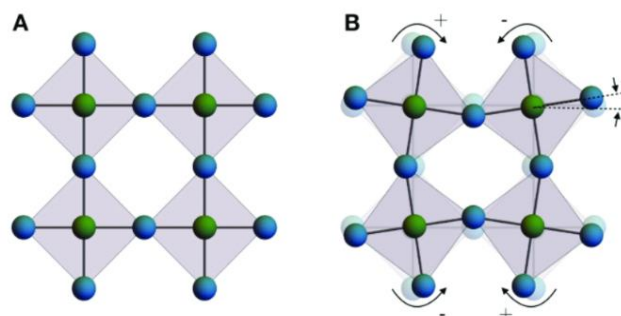


Figure 1.2 (A) 2D layer of model perovskite octahedra. (B) Tilt angle theta showing the constrained motion of neighboring octahedra due to shared inter-octahedral X sites [1]

1.2 Motivation for This Research

My thesis research began by assisting others in the Bio/Organic Electronics lab prototyping a transistor design using MAPbI₃ as the semiconductor. Various experiments ensued using precursors (MAI and PbI₂) in solution, spin-coating an indium tin oxide (ITO) substrate that had been machined forming a nonconducting channel between two ITO pads. The precursors were prepared in solution, according to the recipe from Zhou et al. [41]. Measured amounts of solution were dropped onto the spinning substrate, then heated forming crystal MAPbI₃. Research continued varying the ITO substrate channel design and preparation, its width and depth, varying the angle of the channel from perpendicular to the shape of a “V” where the distance between contacts varied with the change in channel depth. Samples were exposed to varying frequencies of light and electronic measurements taken to characterize the junction.

The process caused the MAPbI₃ to crystallize randomly, forming microscopic cylindrical structures that appeared as needles or asbestos fibers varying in length, diameter and

orientation, resembling an amorphous crystal. Controlling coherent electric contact between the MAPbI₃ and the walls of the ITO, the uniform distribution of MAPbI₃ in the channel as well as the stability of MAPbI₃ proved challenging. Interestingly, reheating a sample with additional precursors would often cause recrystallization. My focus turned toward the process of MAPbI₃ single crystal growth as a method to deposit a MAPbI₃ crystal in the channel, thereby avoiding many of the experimental difficulties. Others have continued developing a capillary method to deposit MAPbI₃ material in the channel with good success [42].

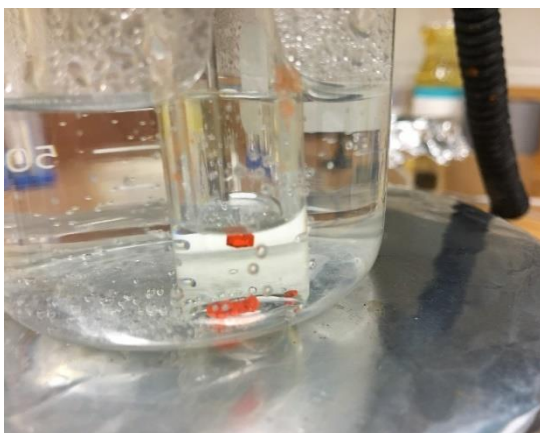


Figure 1.3 Single-Crystal growth in solution



Figure 1.4 Sample MABr₃ single crystal of 5mm grown by ITC

Several methods of producing MAPbI₃ are available [43-47]. One of the methods utilizing Inverse Temperature Crystallization (ITC) appeared the simplest, forming large sized single-crystals suitable for physical measurements. The ITC method is solution based at practical temperatures (90-130 C) using available lab equipment and instruments. The lab experiment shown in Figure 1.3 is a solution process growth of MABr₃ by ITC method in an oil bath at 100 C. The MAPbBr₃ was selected over MAPbI₃ due the lower crystallization temperature (100 C in MAPbBr₃ vs. 130 C in MAPbI₃) and the prototypical regular shape of

MAPbBr₃ with large flat surface. The large single-crystal sample proved easier to handle and provided large flat surfaces for probe placement compared to MAPbI₃. Yet, the physical structure of a central MA molecule constrained by a Pb-Br framework is structurally similar to that of MAPbI₃. There are two sample vials shown on Figure 1.3, the larger single orange crystal is growing in a separate vial behind the vial with several smaller single crystals in the forefront. Both samples grew in 4 hours.

The larger crystal was dried, stored in a nitrogen filled vial in an oven at 100 C for 8 hours. Figure 1.4 shows the results of this particular lab experiment. The crystal is 5 mm, approximately rectangular but showing a dimple caused by the casting of the glass vial. The perpendicular edges form from the bottom up growth and importantly, the growth molds to the containing crystallization vessel. This molding behavior can likely be exploited to grow such a single crystal in an arbitrary shape controlled only by the shape of the reaction vessel. The 5 mm crystal size is sufficient to handle the sample with tweezers and is of sufficient size and shape to easily accommodate four electrical probes to perform basic electronic characterizations – conductivity, I-V plots and sample stability over time.

ITC itself is an unusual process in crystallography. Most natural crystals are formed by cooling a substance. The class of A B X₃ perovskites where site A is methylammonium, site B is lead and site X is I, Br or Cl, all form via ITC. All have similar optical absorber properties but with dissimilar bandgaps varying by cation size and unit cell volume. Importantly, these organic-inorganic perovskites form an inorganic cage surrounding a single methylammonium cation that is not covalently or ionically bound to any other atom, making these class of perovskites

unique. Intuitively, I theorized that the well reported photo properties in MAPbI₃ is due to the unique caged methylammonium structure.

The geometry of the perovskite, the nature and type of hydrogen bonding, the role of the methylammonium cation, the interactions between the organic molecule and that of the inorganic cage, and even the crystal type structure of these perovskites remain unclear and the source of speculation and contradiction in publications. Yet, certain physical properties are without dispute; the chemical formula, and the bandgap for each species is well studied owing to perovskite application in solar cells, among others, most from experimental evidence.

My effort to understand the behavior and underlying processes at work in these perovskites turned to modeling using *ab initio* or first-principle methods of Density Functional Theory (DFT) and derivative functionals extending DFT.

1.3 The Origin and History of Perovskite Development

A Perovskite is a generic structure for a compound like calcium titanate, a compound of a cubic (like) crystal structure. Naturally occurring perovskite compounds are found in igneous rock deposits formed through the cooling and solidification of magma, tectonic uplifting or lava.

Perovskite compounds were first reported by German scientist Gustav Rose in 1839 researching mineral deposits in Ural Mountains of western Russia. Rose discovered calcium titanium oxide CaTiO₃. To honor Count Lev Alekseevich von Perovski (1792-1856) the Russian mineralogist, this mineral was named Perovskite. Some 50 years would pass with little to no published research on perovskites until 1892 when Wells, Campbell, Walden and Wheeler, working at the Sheffield Scientific School in New Haven, CT, produced the first synthetic

perovskite halide from cesium and lead from aqueous solutions. An original paper, print image, in German, Figure 1.5, is believed to be the first paper on lead-halide perovskites.

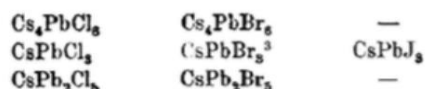
Another 50 years would pass without major published research on perovskites until in 1947 when Phillips at Eindhoven (the Netherlands) demonstrated barium titanate use in the construction of condensers.

Über die Cäsium- und Kalium-Bleihalogenide.

Von

H. L. WELLS.¹

Als Fortsetzung der in diesem Laboratorium² begonnenen Arbeit über Doppelhalogenide ist von den Herren G. F. CAMPBELL, P. T. WALDEN und A. P. WHEELER eine Untersuchung über die Cäsium-Bleisalze unternommen worden. Diese Herren haben die Untersuchung mit vielem Eifer und Geschick durchgeführt, und es macht mir Freude, ihnen meinen Dank auszusprechen. Sie haben die Existenz folgender Salze konstatiert:



Sheffield Scientific School, New Haven, Conn., Oktober 1892.

Figure 1.5 Early publication on lead halide perovskites

Shortly afterwards in 1957, while analyzing the fine structure of compounds produced by Wells at Sheffield, the perovskite crystalline structure was categorized by Moller of the Royal Agricultural College in Copenhagen who published “The structure of cesium plumbo iodide CsPbI_3 ”.

Importantly, Moller also observed photoconductivity in this material. The excerpt from Nature, November 22, 1958 below titled “Crystal Structures of Photoconductivity on Caesium Plumbohalides” (Fig 1.6) [48] is the first reported photoconductivity of a perovskite-based material. The paper outlines the now well-known crystal structure CsPbX_3 using Cesium as the

outer cubic corner atoms and the inner atoms where X molecule is identified as Cl, Br or I, the species under research in this thesis. The same year Siemens (Munich, Germany) produced barium titanate-based resistors. The next four decades saw a wide range of developments using perovskite material, from electronic material to optical, piezoelectric and ceramic materials and more. In 1955

The Western Electric of New York, NY, used ferroelectric crystalline oxides with the characteristic perovskite structure to fabricate electro-mechanical transducers. Two years later in 1957 Clevite utilized perovskites to fabricate piezoelectric resonators for electro-mechanical filters. Then In 1964 Compagnie Générale d'Electricité developed perovskite-based solid electrolytes catalysts used in fuel cells. In 1971 Corning Glass in Corning, NY developed a process using perovskite oxides in frits for glass-ceramic products. The same year Exxon Research Engineering at the Linden labs patented a process that used a perovskite-based cathode catalyst to convert alcohols into ketones.

Weber in 1978, working at the University of Stuttgart, first reported hybrid organic-inorganic halide perovskites. This process replaced cesium cations with methylammonium ions in the original halide compound that was first synthesized by Wells. His work provided guidance for future study into perovskites for solar cells. Since 1978 there have been thousands of research papers on systems with cubic perovskite structures and a great many focused on the study of methylammonium lead halides perovskites. By the middle 1990's several commercial applications of perovskite structures were described. In 1994 Mitzi, working at IBM Yorktown Heights research lab, demonstrated organic-inorganic halide perovskites as light emitting

devices. Two years later, in 1996 Boeing Research demonstrated cesium-germanium halide salts perovskites showing nonlinear optical crystals in optoelectronics.

NATURE November 22, 1958

Crystal Structure and Photoconductivity of Cesium Plumbohalides

WELLS¹ and his collaborators have shown that crystals of the general compositions CsPbX_3 with $X = \text{Cl}$, Br or I , and Cs_2PbX_6 with $X = \text{Cl}$ or Br , may be prepared from aqueous solutions. I have investigated the structures of these crystals and also prepared a few more. I have found² that CsPbCl_3 and CsPbBr_3 have the perovskite structure. At room temperature they are tetragonally or monoclinically distorted. Both of them, however, show transition to pure cubic perovskite structure, at 47° C. and 130° C. respectively and with cell dimensions $a = 5.605 \text{ \AA}$. for CsPbCl_3 , $a = 5.874 \text{ \AA}$. for CsPbBr_3 . Whereas no extra or forbidden X-ray reflexions can be observed above these transition temperatures, CsPbBr_3 below 130° C.—and presumably also CsPbCl_3 below 47° C.—exhibit a new structure corresponding to a doubling of the cell dimensions. The transitions are likely to be of second order as $\Delta V = 0$ within the limits of accuracy of my measurements.

It is interesting to note that the above-mentioned crystals with perovskite structure are intensely coloured: CsPbCl_3 is pale yellow, CsPbBr_3 is orange and CsPbI_3 black, whereas crystals of the type Cs_2PbX_6 with $X = \text{Cl}$, Br or I are colourless. From this peculiarity one might guess that the former crystals also have special electrical properties. With a very crude apparatus we have found that the coloured CsPbX_3 -crystals with perovskite structure are photoconductive, CsPbCl_3 having its maximum spectral sensitivity in the violet, CsPbBr_3 in the blue to green region and CsPbI_3 in the red region, that is, the spectral region which is complementary to the colour of the crystals.

A detailed account of this work will be published elsewhere.

CHR. KN. MØLLER

Chemical Laboratory,
Royal Veterinary and Agricultural College,
Copenhagen.

¹ Wells, H. L., *Z. anorg. Chem.*, **3**, 195 (1903).

² Møller, C. K., *Nature*, **180**, 981 (1957).

Figure 1.6 Publication in Nature, Wells, H. [48]

In 1999, Chikao at the NIAIST in Tokyo Japan, demonstrated a fabrication method for an optical absorption layer for solar cells using rare earth perovskite compounds. Since then substantial worldwide research is devoted to the commercialization of perovskite-based solar cell technology.

In 2008 an early paper, Figure 7 (below), if not the first, on lead-halide perovskite compounds ($\text{CH}_3\text{NH}_3\text{PbBr}_3$) was presented at the 214th ECS Meeting, Abstract #27, at the Electrochemical Society meeting October 12 - 17, 2008, Honolulu, Hawaii [49]. Figure 1.7, shows the ideal chemical structure (but not the actual geometry as discussed in Chapter 2) of a perovskite unit cell.

The unit cell is a “box” of 8 NH_3 atoms in an idealized cube containing a molecule of 6 Br atoms with a single Pb atom covalently bonded. The ions depicted to the right in this graphic

show the charge, hence the unit cell is charge balanced. All perovskite materials follow this idealized crystal geometry, shown in “Fig. 1 $\text{CH}_3\text{NH}_3\text{PbBr}_3$ ” (above). Discussed in Chapter 2, this lead-centered unit cell is not geometrically accurate and the unit cell shape is greatly influenced by thermal activity. This thesis suggests an alternative view of the perovskite structure model, one where the MA is centered in a dynamic lead-iodide framework. The MA is not ionically bound to the framework but is free to rotate and revolve in reaction to changes in the Pb-I frame and from external energy. An important assertion in this thesis is the Pb-I frame is not fixed or ridged, as that of a hard-crystalline lattice like silicon. This thesis presents the center-centric MA cation as a free molecule able to rotate, spin and tumble in three dimensions, influenced by deformations in the elastic Pb-I framework.

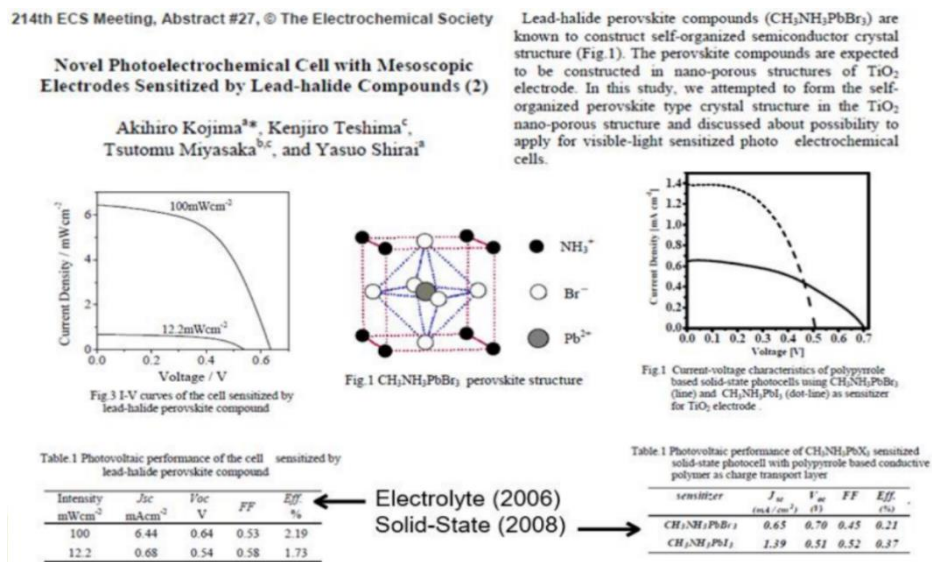


Figure 1.7 Image from Kojima, A., 214th ESC Meeting, Abstract #27 Paper [49]

1.3.1 Perovskites Photovoltaic Applications

Highly motivated to find new and improved methods to harvest solar energy by photovoltaic conversion, science and industry have embraced perovskite materials for use in solar cells as viable option to compete with more conventional silicon-based devices. The recent entry of demonstratable perovskite devices and the rapid improvement in the efficiencies of these perovskite cells has garnered much research and development of commercial photovoltaic cells.

The National Renewable Energy Laboratory publishes and updates their “Best Research-Cell Efficiencies” graph regularly, Figure B.1, an excerpt from which is shown in Figure 1.8. This graph illustrates the state of PV cell development since 1975 showing the different technologies over time along with the measured efficiencies. Since 1975 PV cell efficiencies for thin-file ranged from 9% while single crystalline Si cells range in the 13%-14%. As expected, PV efficiencies steadily grew over time and new PV technologies entered the market. As of August, 2020, Thin-Film and Crystalline-Si cells have reached 23% (in green) and 27% (in blue) respectively. Omitted are exotic and expensive multijunction (and multilayer) cells (in purple) as these are not yet commercially viable. Noteworthy is the rapid speed of perovskite-based cell development relative to all cell types. With the first entry of a perovskite-based cell introduced in 2013 with an efficiency of 13% to the most recent entry of a perovskite/Si tandem cell at 28% efficiency in 2020, no other technology has achieved such a rate of efficiency improvement. In a mere 6 years, perovskite-based PV technology has demonstrated efficiency improvements taking over 30 years for other technologies. Little wonder perovskites have emerged as a prime topic of research.

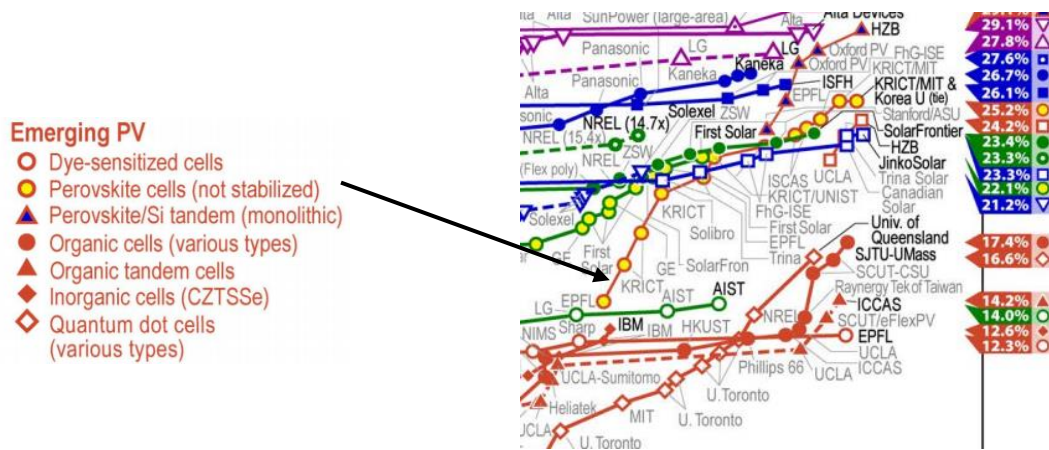


Figure 1.8 Perovskites inset of NREL Best Research-Cell Efficiencies as of 08/03/20. Courtesy of the National Renewable Energy Laboratory, Golden, Colorado.

Noteworthy is the rapid speed of perovskite-based cell development relative to all cell types. With the first entry of a perovskite-based cell introduced in 2013 with an efficiency of 13% to the most recent entry of a perovskite/Si tandem cell at 28% efficiency in 2020, no other technology has achieved such a rate of efficiency improvement. In a mere 6 years, perovskite-based PV technology has demonstrated efficiency improvements taking over 30 years for other technologies. Little wonder perovskites have emerged as a prime topic of research.

Motivated by the fast-growing market for perovskite solar cells, in this thesis I focused on simulating MAPbI₃. Chapter 2 reviews several computational functionals, identifies their strengths and weaknesses as applied to calculation, the electronic band structures, atomic volume and band gap of MAPbI₃. Chapter 3 introduces a method to extend the current functionals by exploiting commonality between adjacent unit cages that improves computational efficiency. This in turn allows for larger supercells to be considered, reducing the averaging error induced by functional approximations and reduces the fringe effects at the supercell boundaries. Chapter 4 summarizes the findings and compares the results from

traditional functional methods with those presented in Chapter 3, and lastly, suggests avenues for future study.

Chapter 2: Computational Material Science Methods

2.1 Background of Existing Methods

Historically, science has evolved following two paths, the theoretical and the practical. Theorists focused on developing principles that describe natural phenomena derived from the mathematical expressions of the discipline. Experimentalists designed and performed tests to obtain results and validate the expression of theories. In the early 20th century, new theories by Schrödinger, Dirac and many others [49], emerged to explain the fundamental properties of matter at the atomic scale. Quantum mechanical models require solving intricate and difficult mathematical systems of equations, often iteratively, solving systems that describe the interaction of particles. Owing to the number and complexity of calculations involved, many theoretic postulates remain untested.

With the advent of digital computers, researchers can take advantage of computing speed and emerging efficient algorithms to perform the necessary calculations. Research universities have developed code for mathematical problems in theoretical chemistry [50-52]. Advancements in computational chemistry has been influenced both by the computational speed of computers and the evolution of theories, often both intertwined. The computational complexity of most quantum mechanics and related disciplines requires a large amount of computing power and large storage space, which are the limiting factors of computers.

Modern computing platforms have been designed to support clusters of physical computers with multiple machines per cluster and multiple CPUs per machine. Fortunately,

computer science has evolved rapidly to the point where supercomputers are able to manage the complex mathematical algorithms required to simulate large molecular models. The study of solid-state physics and electronic properties of matter is influenced by the availability of computational chemistry. With the current available computing technologies and advanced software [53, 54], we are able to simulate molecular structures of complex materials such as proteins. Yet, not much effort has been dedicated to simulation of organohalide perovskite materials, perhaps due to the assumption of simplicity in their crystalline structure [55]. In this Chapter we review various common models that have been used for studying the molecular structure of chemicals. The limitations in each model have been emphasized to justify the need for a different computational model to be used for studying MAPbI₃.

2.2 Force Field Molecular Model

Basic to all computational methods is the idea of determining the molecular geometry of a molecule. Force field (FF) methods were one of the first computerized computations owing to the relatively low computer power requirements. Given a set of atoms or molecules and the bonds between atoms and their attraction and repulsion of charges, force field calculation determines the geometrical location of the atoms that minimizes the potential energy of the system [56, 57]. The method assumes the system is at 0 K, in a ground state configuration, and treats all particles as point charges. The force field algorithm analyzes covalent and noncovalent bonds, bond lengths, bond angles, torsions, electrostatic, van der Waals forces and polarizability. Bond stretching is used to vary bond length often using the mechanical analogy of Hook's law for springs.

Force field algorithms methods are designed to find the global minimum energy of the system by iteratively changing the geometry of particles and their charge optimizing the entire system to an acceptable error margin [58]. Convergence can reach one thousandth of an angstrom. Simple algorithms treat each atom as a point source while more sophisticated algorithm include interrelated elements of the atom, proton and electron orbitals charge-space and long-range electrostatic force.

Many programs for building and visualizing molecules include at least some degree of force optimization. Avogadro [59] is a PC-based graphics program that supports GAFF, MMFF94, MMFF94s, Ghemical, UFF methods, and provides the steepest descent and conjugate gradient algorithms. The force field algorithms are simple and can be used for molecular optimization in real time as part of the graphical interface of the program. Using consumer grade PC with Intel i7 cores, complex molecules consisting of more than 128 atoms can be optimized in less than a minute.

With the exception of the simplest molecules, force field models are inaccurate due to the empirical derivations. Defects include the failure to account for anisotropic charge distribution, environmental electronic polarization, dielectric constant, dipole moment, and quantum effects [60]. However, the force field model plays an important role in quantum chemistry. Many sophisticated modeling techniques will benefit from a rough initial condition calculation, i.e., a molecular model that most accurately represents the molecule studied starts by using a force field model.

2.3 Schrödinger Equation

Of particular importance in the evolution of computational methods is the contribution of Edwin Schrödinger. In 1926, Schrödinger proposed the wave behavior of particles as a linear partial differential equation (PDE) representing the wave function (or states) of a quantum mechanical system [61]. The Schrödinger equation relates the temporal evolution of quantum particles as waves in the time-dependent general form:

$$i\hbar \frac{\partial}{\partial t} |\psi(t)\rangle = \hat{H} |\psi(t)\rangle,$$

where unit imaginary number (i), \hbar (h-bar) is the Dirac constant, which is the reduced Planck constant developed by Bohr, $\hbar = \frac{h}{2\pi}$ as the quantum of angular momentum, ψ is the wave function (quantum system), t is time, and \hat{H} is the Hamiltonian operator representing the set of energy values of the system [62]. The Hamiltonian operator is a linear transform that acts on functional spaces. The meaning of the Hamiltonian operator is the equivalent idea of eigenvalues of a matrix. Therefore, the solution of a problem is often specified as eigenvectors and the corresponding energy eigenvalues. The solution of the equations is the state of the system. When all of the lowest energy orbitals are occupied, the system is in the ground state as codified in Hund' rules [63]. This general solution does not place any constraints on the system.

My research is concerned with the behavior of methylammonium lead iodide perovskite (MAPbI₃) in solid-state crystal form as an electronic material. The commonly used time-independent form of the Hamiltonian $\hat{H}\psi = E\psi$, solving for $H = \left[\frac{-\hbar^2}{2m} \nabla^2 + V(\mathbf{r}) \right]$. The Hamiltonian is composed of kinetic energy and potential energy for a system composed of M

nuclei and N electrons. The explicit form of the Hamiltonian [64] can be expressed as:

$$\hat{H} = -\frac{\hbar^2}{2m} \sum_{i=1}^N \nabla_i^2 - \frac{\hbar^2}{2} \sum_{\alpha=1}^M \frac{\nabla_{\alpha}^2}{M_{\alpha}} - \sum_{\alpha=1}^{M,N} \frac{Z_{\alpha} e^2}{|r_i - R_{\alpha}|} + \sum_{\alpha=1}^{M,N} \sum_{j < \alpha} \frac{e^2}{|r_{ij}|} + \sum_{\alpha=1}^{M,N} \sum_{\beta < \alpha} \frac{Z_{\alpha} Z_{\beta} e^2}{|R_{\alpha} - R_{\beta}|} \quad (1)$$

where R and r are the nuclei and electron coordinates, respectively. Since each term is an energy, the equation can be simplified into terms of a function of electrons, r and atomic positions, R :

$$\hat{H}(r, R) = \hat{T}_e(r, R) + \hat{T}_N(r, R) + \hat{V}_{e-N}(r, R) + \hat{V}_{e-e}(r, R) + \hat{V}_{N-N}(r, R) \quad (2)$$

The first term represents the kinetic energy of electrons, the second the energy of the nuclei.

The remaining three are potentials that describe the interactions between electrons-nuclei, electrons-electrons and nuclei-nuclei, respectively.

The Schrödinger equation gives exact solutions only for nuclei with one electron[61].

The Schrödinger equation alone cannot provide practical methods for analyzing complex atoms or molecules although Schrödinger's work is the basis for subsequent theories and methods.

The Hamiltonian in equation (1) is a direct result of the Schrödinger equation. Equation (2) is a simplification of the equation (1) and thus can only exactly solve for a single electron. All is not lost. Other methods expand on the Schrödinger equation method by using approximations instead of an exact solution [65]. The rest of this section describes the methods currently used in quantum chemistry, with a focus on the methods used in this research.

In classical mechanics, the Hamiltonian is a scalar function. In quantum mechanics, it is an operator on a space of functionals where the eigenvalues of \hat{H} is the energy of the system.

Derivation of the Schrödinger equation involves the Dirac-von Neumann axioms [66] and wave

functions representing unit vector defined on a complex Hilbert space. Certain conditions must exist derived from the unitary¹ principal [67, 68], all of which are beyond the scope of this research.

Practical computational methods generally involve modifying the Hamiltonian operator in ways to extend the capability of quantum methods or improve the algorithmic performance by relying on specific situations that exist in the system, such as molecular symmetry or reduce computation complexity by asserting mathematical approximations [69]. The various quantum computational methods described below all build on the foundational Schrödinger equation to improve accuracy or computational efficiency.

2.4 Born–Oppenheimer Approximation

Building on the Schrödinger equation, in 1927, Max Born and J. Robert Oppenheimer proposed the motions of electrons and atomic nuclei be treated separately. The Born–Oppenheimer approximation realized there is a large difference in the mass of the nuclei compared to the mass of the electrons, a ratio on the order of 0.1%, hence a proportional difference in the timescale of their motion [70]. For the same kinetic energy, the nuclei being much more massive move much more slowly than electrons. Still, the total wavefunction is the product of nuclear vibrational and rotational wavefunctions and that of the electronic wavefunctions, $\Psi_{Total} = \Psi_{nuclear} * \Psi_{electronic}$. Now, the Hamiltonian operator is separated into nucleus and electron terms and we neglect the relatively small cross terms between them. The total energy of the system is the sum of the electronic + vibrational + rotational +

¹ In quantum physics, unitarity is the condition that the time evolution of a quantum state according to the Schrödinger equation is mathematically represented by a unitary operator.

nuclear spin energies, where the terms differ in orders of magnitude. Compared to other terms, the nucleus spin energy is insignificant and can be ignored, further simplifying the calculation. Neglecting the nucleus spin energies is not always prudent as this energy plays an important role for some systems and plays a role in MAPbI₃.

Neglecting the cross product causes the calculations to be approximated. The benefit of the two smaller, decoupled systems is that the two systems can be more efficiently solved than the original Hamiltonian. Terms included in calculating the electron energy structure of a molecule include kinetic energy, dielectric repulsion, inter-nucleus repulsion, and electron attraction. In modeling, when the nuclei move, the solution changes, but the electron rearrangement occurs almost immediately, forcing a new ground state but without affecting the motion of the nuclei.

The method is a two-step process. First, we find the electronic wavefunction with the nuclei coordinates as parameters, then subtract the kinetic energy T_n from the total Hamiltonian. This results in the electron Hamiltonian H_e in which the nucleus position becomes a constant parameter, but the nucleus-electron interactions are retained. The Coulomb potential on the nuclei and electrons exists and is clamped at certain points in space. In the second step, the electronic eigenvalues, representing the nucleus energy T_n that was removed in the first step, is now returned, then the Schrödinger equation with small displacements of the nucleus coordinates is solved iteratively.

The Born–Oppenheimer approximation is based on several assumptions [71]. One is that heavy nuclei move more slowly than light electrons. The method ignores that lower-orbiting electrons travel at speeds close to the speed of light, implying relativistic properties.

The electronic energy depends on the initial position of the nuclei. Vibration coupling and other issues are addressed in subsequent sections.

2.5 Hartree Electron Position Approximation

The electronic wavefunction analysis depends on locating the position of each and every single electron in the system. Building on the Schrödinger equation and combining it with self-consistency introduced by Lindsay, Hartree proposed that the nuclei, along with the electrons, could be treated as a spherically symmetric field [72]. Mathematically, $\psi = \psi_i(\mathbf{x}_1, \mathbf{x}_2 \dots \mathbf{x}_n)$ where \mathbf{x}_i is the electron position and spin of the i^{th} electron. Assuming the interaction between electrons, $\hat{V}_{e-e(r)}$ is constant, then the Hamiltonian is the sum of all the independent single electron Hamiltonians. Hence, the electronic wavefunction of the system can be written as:

$$\hat{H}_e = \sum_{i=1}^n \hat{h}_{e,i}, \text{ then, } \psi_e(\mathbf{x}_1, \mathbf{x}_2 \dots \mathbf{x}_n) = \prod_{i=1}^n X_i(\mathbf{x}_i)$$

The solution of the Schrödinger equation is the electron charge density in time and space for each electron in the potential field. Self-consistency requires that the final field calculation be self-consistent with the first field. Hartree converts physical units to atomic units. This change base eliminates the physical constants, and converts the Laplace operator from Cartesian to spherical coordinates. This transforms the system to radial functions with spherical harmonics with an angular quantum number.

Hartree function is not enough to describe the multi-particle wave function as a combination of independent wavefunctions. Electrons are fermions, that must be represented by antisymmetric wavefunctions, $\psi_e(\mathbf{x}_1, \mathbf{x}_2 \dots, \mathbf{x}_i, \mathbf{x}_j, \dots \mathbf{x}_n) = -\psi_e(\mathbf{x}_1, \mathbf{x}_2 \dots \mathbf{x}_j, \mathbf{x}_i, \dots \mathbf{x}_n)$ [73].

2.6 Hartree-Fock Equation

The Hartree–Fock (HF) approximates the energy of the wavefunction for the base state of a system. HF is also called the self-consistent field method (SCF). The HF method is predicated on the assumption that an approximation of the electronic wavefunction is available using the Slater determinant. Solving these equations produces the HF wavefunction. To ensure the antisymmetric wavefunction, the HF equation incorporates the Slater determinant along with the Pauli exclusion principle. The antisymmetric wave function can be described mathematically using the Slater determinant [74]. A property of determinants is that any permutation of matrix rows or columns causes a change in the sign of the matrix determinant. For the general case of an n-electron system, the well-known Slater determinant is defined:

$$\Psi(x_1, x_2, \dots, x_i, x_j, \dots, x_n) = \frac{1}{\sqrt{n!}} \begin{vmatrix} X_1(x_1) & X_2(x_1) & \dots & X_n(x_1) \\ X_1(x_2) & X_2(x_2) & \ddots & X_n(x_2) \\ \vdots & \vdots & & \vdots \\ X_1(x_n) & X_2(x_n) & \dots & X_n(x_n) \end{vmatrix}$$

Using the Slater determinant to resolve the prerequisite antisymmetric property, what remains is to calculate the single electron wavefunctions. The energy ϵ for the system is given by:

$$\epsilon = \langle \phi | H_e | \phi \rangle = -\frac{\hbar^2}{2m} \sum_i \langle \psi_i | \nabla_i^2 | \psi_i \rangle + \sum_i \langle \psi_i | \nabla_i^2 | \psi_i \rangle$$

The first term represents the Coulomb contribution between electrons. The second term accounts for the exchange interaction resulting from asymmetry of the Slater determinate and Pauli exclusion.

Expanding the Slater determinant and using Lagrange multipliers for minimization, the resulting equation, along with the restrictions of normalization, results in the HF approximation, more recently called the self-consistent field method (SCF) [75]:

$$\left(-\frac{\hbar^2}{2m}\nabla^2 + u_{est}\right)|\psi_e(\hat{r})\rangle + e^2 \sum_{i \neq j} \int \frac{\psi_j^*(\hat{r})\psi_j(\hat{r})}{|\hat{r} - \hat{r}^*|} d\hat{r} |\psi_i(\hat{r})\rangle - \int \frac{\psi_j^*(\hat{r})\psi_i(\hat{r})}{|\hat{r} - \hat{r}^*|} d\hat{r} |\psi_j(\hat{r})\rangle = k_{ii} |\psi_j(\hat{r})\rangle$$

HF theory was developed to solve the electronic time-independent Schrödinger equation, after application of the Born-Oppenheimer approximation. The HF relates the exact many-body wavefunction approximated by a single Slater determinant. When all single electron solutions are computed, it is possible to calculate the energy structure of the system. The HF simplification and assumptions introduce several weaknesses. Most importantly, ignoring the electron correlation increases the deviation from experimental results. Several post-Hartree-Fock methods aimed at solving or minimizing these shortcomings are described below, including the correlation between multiple electrons, Møller-Plesset perturbation theory [76], and variable component Monte Carlo [77].

The HF results in a single determinant wavefunction that takes into account exchange interactions from antisymmetric of the wavefunction. However, there are several drawbacks as the methods ignore interactions between electrons with opposite spin.

There is a significant computational expense to solve the HF equations on the order of $O(N^4)$, for N elements in the base set. A number of computation approximations can reduce this cost to $O(N^2)$ but these approximations introduce significant error [78]. This scaling makes the HF method impractical for large systems.

2.7 Hartree-Fock and Linear Combination of Atomic Orbitals

The Linear Combination of Atomic Orbitals (LCAO) method develops an atomic orbital model based on the known shape of orbitals whereas the HF model operates by optimizing the shape of the orbitals themselves. This method creates a model that is more qualitative than the HF quantitative model [79].

Consider an H_2^+ molecule. The two protons of the nuclei are very far apart. The ground state electron is an $1s$ orbital about one of the protons, but we do not know which proton. From Schrödinger's cat paradox there is some probability the electron orbits around one or the other. Just as with the HF method, the LCAO method proposes an estimate of the wavefunction for the electron as the sum of a constant multiplied by the wavefunction of the electron based on the location of the electron relative to proton. The process occurs for each electron matched to a proton as described above. The assumption is that a $1s$ electron orbital is centered on a proton and a second $1s$ electron orbital centered on another proton and so on. The spherical coordinate system uses (r, ϕ, θ) for the position of the radii, allowing the positions to be simply expressed. The goal is to find values of the coefficients for each electron-proton pair that optimize the amplitude for the electron found around the proton.

This description pertains to a single H_2^+ , however, this orbital based approach applies to larger, more complex atoms and molecules with higher orbitals. In general, the model assumes a one to one correspondence between the number of molecular orbitals and atomic orbitals. Calculating the coefficients of the linear combination of terms is computationally effective, resulting in a linear combination of one-electron functions. Interestingly, these results may not

be centered on any specific nuclei. Yet, the LCAO method result is two wavefunctions (for H_2^+), and in general, N wavefunctions for an N atomic orbitals.

An alternative approach is Density Functional Theory (DFT), which treats both exchange and correlation energies by approximations. These are hybrid functions that combine the HF and DFT methods. Recent research has developed the valence bond theory, which is computationally comparable to the HF method in accuracy and efficiency. Overlapping atomic orbitals are replaced by superposition of linear combinations of basis functions, thereby forming a LCAO which is then optimized by truncating orbitals beyond a certain distance, typically past the mid-point of the second nearest neighbor, to give an approximation of the lowest energy [80].

2.8 Density Functional Theory

The HT method is computational complexity, linearly related to the number of dimensions (variables) of the system, for example the number of electron coordinates for all electrons of the entire system. Density Functional Theory (DFT) method is an *ab initio* calculation that models the electronic structure of a system as a many-body system, principally atoms and molecules in the condensed state. DFT can calculate the ground state properties and predict many molecular properties such as the geometric structure, vibrational frequencies, energy bands, bond length, angles and torsions, bonding energies of ionization and atomization and electronic parameters.

The molecular properties of materials can be determined by using functionals. In DFT, functionals are functions of other functions. This process is similar to, but not precisely, the mathematical composition function, (*fog*). The main focus of this method is to determine the

spatially dependent electron density [81]. DFT has become one of the most commonly used methods in solid-state modeling, yet this method has several shortcomings dealing with intermolecular interactions related to van der Waals forces and the modeling of exchange and correlation interactions [82]. Neglecting these interactions lead to inaccurate calculations of potential energy surfaces, band gaps, and ferromagnetism in semiconductors and crystals, which are the subject of this study

DFT is based on theorems proposed by Hohenberg and Kohn (H-K) [83] in the mid 1960's that allow the Hartree-Fock function, with its large number of variables, to be replaced by a single function that depends on only three spatial coordinates, $(n, (x, y, z))$. Subsequently, H-K theories were expanded to encompass both non-degenerate and degenerate ground states in strong magnetic fields [84].

Their first theorem shows that the ground state of a many-body electronic system is defined by the electron density of the system, $n(\mathbf{r})$, in a three-dimensional coordinate system (x, y, z) . In DFT terms, the ground state of electronic system is termed the functional of the electron density. A DFT functional is a mathematical operator taking a function as an argument and returning a value. The H-K theories have been expanded to address the time dependent density functional theory (TDDFT). This aspect of the model describes the excited states. The second H-K theorem addresses the consistency of the theory at ground state. That is, the functional that calculates the lowest energy of a system is defined as the ground state density functional. This is a mathematical closure problem. More simply, when the charge density of the system is at ground state, the Hamiltonian energy is a global minimum [85].

Many follow-on methods build on the DFT method to improve the accuracy and extend the capabilities of the model. These replace the functionals of DFT or TDDFT and therefore, understanding the underpinning of DFT provides the base to appreciate the post-DFT methods.

The KS effective potential is defined as:

$$u_{eff}(\vec{r}) = u_{ext}(\vec{r}) + \frac{\delta J[\rho]}{\delta \rho(\vec{r})} + \frac{\delta E_{xc}[\rho]}{\delta \rho(\vec{r})} = u_{ext}(\vec{r}) + \int \frac{\rho(\vec{r}')}{|\vec{r} - \vec{r}'|} d\vec{r}' + u_{xc}(\vec{r}) \quad (3)$$

where $u_{xc}(\vec{r})$ is the exchange correlation energy:

$$u_{xc}(\vec{r}) = \frac{\delta E_{xc}[\rho]}{\delta \rho(\vec{r})} \quad (4)$$

Restricting the Euler-Lagrange to the density of N particles,

$$\int \rho(\vec{r}) d\vec{r} = N$$

is the DFT approximation for a system of non-interacting electrons that are moving in an external potential field $u_S = u_{eff}(\vec{r})$ in (2.1). Substituting this into equation (1) is the solution for the density function $u_{eff}(\vec{r})$, equation and is the solution of N one-particle equations:

$$\left[-\frac{\hbar^2}{2m} \nabla^2 + u_{eff}(\vec{r}) \right] |\psi_i\rangle = \epsilon_i |\psi_i\rangle \quad (5)$$

With substitutions from above, the basis of orbitals density equation for an N one-particle system:

$$\rho(\vec{r}) = \sum_{i=1}^N \sum_s |\psi_i(\vec{r}, s)|^2 \quad (6)$$

Equations (3-6) are the K-S method of recasting a complex many-body system of interacting electrons in a static external potential into a computationally efficient system of non-interacting

electrons moving in an effective potential field. This method accounts for the external potential, the Coulomb interaction effects between electrons and the exchange-correlation (XC) interactions between electrons. Modeling of the exchange-correlation interactions within the KS method is computationally complex and the local-density approximation was introduced to address this issue.

2.9 Generalized Gradient and Hybrid Approximations

The Generalized Gradient Approximation (GGA) extends the Local-Density Approximation (LDA) to include density information about the gradient of charge density at each point, $\nabla p(\vec{r})$ and includes non-homogeneous electronic density [86]. The general gradient approximation for the energy exchange-correlation equation is:

$$E_{XC}^{LDA}[\rho] = \int p(\vec{r}) \epsilon_{XC}(p(\vec{r})) d\vec{r} \quad (7)$$

where the exchange energy gradient terms of α and β are directional to the particle. Another method by Perdew-Becke-Perdew (PEB) [87] describes a different hybrid functional by combining the Kohn-Sham equation and the generalized gradient equation with a curve fitting factor alpha (α):

$$E_{XC}^{hyb} = \alpha E_X^{KS} + (1 - \alpha) E_{XC}^{GGA} \quad (8)$$

where the first term is exchange energy of the exact Kohn-Sham wavefunction along with the energy of the generalized gradient energy approximation, whereas the two energy terms are proportioned by α , an interactively calculated variable to produce the optimal (lowest) total energy.

All the DFT functions described are not sufficient to describe systems with rapidly changing electron density [88]. An example is a system where van der Waals energy interacts with nearby particles. Another is near the surface interface where the effects of electronic structure vanish into the vacuum. Still, DFT methods are presently the most successful approach to analyze the electronic structure of matter. The DFT functionals have been expanded with approximations to incorporate important characteristics such as electron Spin-Orbital Coupling (SOC), relativistic effects, free energy, excited states, temperature and vibrational properties [89]. Accounting for this phenomenon requires more complex functionals adding to the computational complexity, increasing compute time. Planewave Pseudopotentials is a method to extend the DFT while reducing calculations.

2.10 Planewave Pseudopotentials

The DFT methods described above, including the extensions such as LDA and hybrid functionals, operate on the complete set of particles in the atom, often treating the nucleus as a unit but calculating the position, movement, SOC, potential and kinetic energies of each electron separately. As the number of atoms in a system grows and for system with heavy atoms, the number of particles to track grows. The DFT calculations involve computing the energy interaction of each particle over time and space. The computational complexity grows exponentially, on the order of $O(N^4)$ where N is the number of particles of the system. For even relatively small systems containing a few dozen atoms, calculating the wavefunction becomes prohibitive. The wavefunction oscillates rapidly near the nucleus, posing a particular problem to model requiring more and finer spatial Fourier analysis to preserve accuracy.

Hans Hellmann in 1932 [90] first suggested an alternative, a radically different method from the all-electron DFT method and later Phillips-Kleinman in 1959 [91] focusing on crystal wavefunctions. This approach involves two different approximations, the frozen-core and substituting pseudopotentials for real energy potentials [92]. The frozen-core models the electrons as two separate groups, the core and valence. Its premise is based on the assertion that valence electrons participate in bonding and characterize the reactive properties of the atom while the non-valence electrons, i.e. the core-electron atoms do not. The motion of the core nucleus and non-valence electrons are replaced with an effective potential, modifying the Schrödinger equation to operate with the effective potential and not the original Coulombic potential term. The wave equation can be recast to include the core-electrons as fixed electron contributions and along with the nucleus, allows this portion of the atom to be precalculated and remain fixed throughout the simulation. The valence electrons, treated separately from the core-electrons, are free and participate in the normal DFT calculations.

The atomic pseudopotential energy model replaces the real potential energy as an effective potential but with many fewer particles. This leads to much lower computational complexity in simulations, however, not without drawbacks. Pseudopotentials are designed to mimic the real potential but only beyond a certain radius from the nucleus center. Within this radius the real wavefunction oscillates and is therefore difficult to represent as planewaves. The pseudopotential replaces this high oscillation with a fictitious smoothed wavefunction that approximates energies close to the nucleus. For distances greater than a cutoff distance, r_c , the pseudopotential correlates with the real wavefunctions. Figure 2.1 [93] illustrates the regions adjacent to the r_c transition. The blue dashed lines are the real potential and wavefunction. The

solid red lines show the pseudopotential and pseudo-wavefunction. The selection of the cutoff distance is somewhat arbitrary and is set by the particular pseudopotential definition. Since the core and valence components are determined independently, the pseudopotential designer is free to incorporate whatever approximation algorithm best fits the intended model. This allows further refinement of the values to more closely achieve the real values. The selection of the cutoff radius is also a parameter available to the pseudopotential designer.

Many pseudopotential libraries are freely available from reputable and vetted by many researchers [94]. The pseudopotential for most atoms in the periodic tables, except the very heavy atoms, are precalculated using various methods and with a range of computational accuracy, accounting for various precision and truncation errors. The pseudopotential libraries used in this research are listed in Table 1.

Table 1 – Pseudopotential libraries

Library	Name	URL Link
1	Standard solid-state pseudopotentials (SSSP)	https://www.materialscloud.org/discover/sssp/table/efficiency
2	Pseudo Dojo	http://www.pseudo-dojo.org/index.html
3	Vanderbilt Ultra-Soft Pseudopotential	http://www.physics.rutgers.edu/~dhv/uspp/

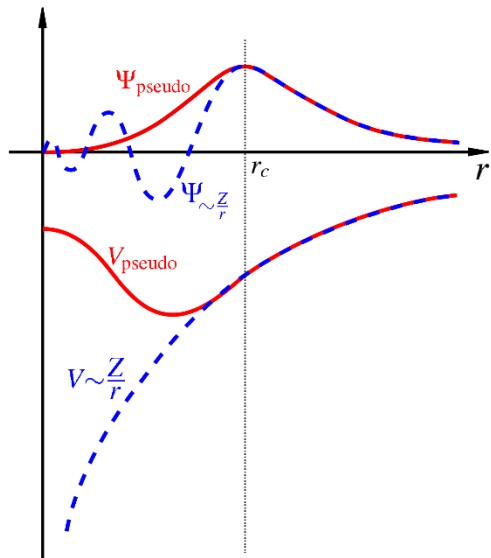


Figure 2.1 Pseudopotential and pseudo-wavefunction comparison. r_c is the cutoff radius where the two correlate [94]

Chapter 3: Computational Methods Results

Chapter 3 reports the method used to construct the MAPbI₃ molecule, develops the relational behind the need to analyze a supercell as opposed to a single unit cell, and reports the results from several DFT methods and the molecular model is developed. The computer modeling software selected to perform the DFT studies is Quantum ESPRESSO (QE) [54].

Quantum ESPRESSO (QE) [54] is a framework supporting a set of Open-Source computational programs to analyze and model the electronic-structure and calculate materials modes at the nanoscale. QE is based on *ab initio* methods of density functional theory and has been extended to support plane waves, and pseudopotential algorithms. The QE distribution consists of source code, freely distributed, with core set DFT implementations and extensions that implement advanced algorithms. The bulk of this package is written in Fortran90. Since the source code is freely available, inspection provides the details of algorithm implementation, the data structures and computational steps employed to optimize the molecular structure and energy, performs the computations and allows one to follow the iterative workflow optimizations.

The primary input data for computation DFT analysis is the list of each atomic species (N, C, Pb, I, H) and Cartesian coordinates of each atom site x, y and z. Method control parameters are provided specific to the Functional and provide symmetry space group specification if appropriate, cutoff energy target to stop the simulation, k-point grid specification, electron occupations methods and lattice structure, among other control

parameter. Using QE, as with most modern DFT packages, is provided in a CRLF separated text file using a combination of keyword parameters and inline data constants.

3.1 Force Field Optimized Model

In general, all molecular modeling tools require as input a definition of the atomic elements and their bonds, along with parameters specific to the tool and the specific modeling method. For this study, Avogadro [59] was selected as the application used to create the perovskite atomic structure and the source of the figures presented herein. The molecule is created manually, atom by atom, using Avogadro 's graphic interface. These 64 atoms with 72 bonds model shown in Figure 3.1a depict the 3D orthorhombic illustration ubiquitous in literature and similar to that in Figure 2a. The supercell was Force Field (FF) geometry optimized, using the Universal Force Field method (UFF). This method adjusts the atomic center to generate the lowest energy based on fixed nuclei size, charge and electron cloud. While far from a quantum mechanically accurate structure, this method provides a fast and convenient method to create a structure useful as input to other tools.

The supercell is shown in Figure 3.1 and 3.1b, conforming to the ABX_3 class of perovskites, with 12 lead atoms, each at the *B* site, at the center of the obscuring silver polygon. Iodide atoms are shown in magenta at each of the 6 corners (corner sharing *X* site) of the polygon. For clarity, the MA cation is omitted from Figure 3.1a and 3.1b, thus showing only the inorganic framework of the perovskite. Notice the high symmetry between the 12

octahedrons. Figure 3.1b is the same molecule as Figure 3.1a but with the polygon adornment removed. This reveals the alternating Pb-I atoms and their bonds.

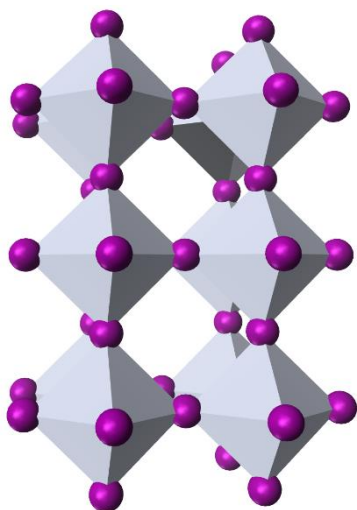


Figure 3.1a Orthorhombic MAPbI₃ created atom by atom with MA cation omitted. Iodide atoms in magenta, lead atoms within the center of the silver polygons

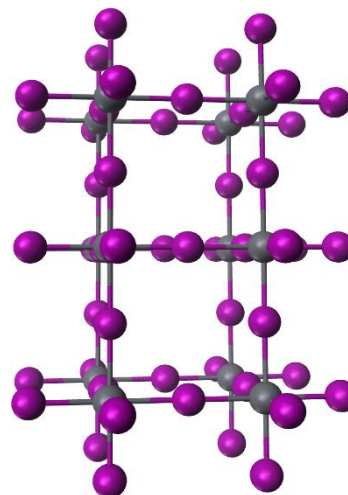


Figure 3.1b Orthorhombic MAPbI₃ without polygons. Iodide atoms in magenta, lead atoms shown in gray

Examining the FF optimized results, bond angles range from 178.4° to 179.6° between any adjacent Pb-I atoms as measured with the Avogadro visualizer program [59]. In the bulk, far away from any boundary, these angles would be 180° as the charged anions are in equilibrium with all the other equally spaced anions, cancelling any charge. In the molecule of Figure 3.1b the structural deformation at the outer boundaries is due to the dangling iodide that repels one another which induces a torque on the connected atoms within the frame. These anomalous boundary charges pose a significant obstacle to DFT analysis as they artificially skew the interactions occurring nearby to the surface but within the bulk. An obvious remedy is to increase the supercell size so the boundary atoms effect within the bulk is reduced. However, as the supercell size increases, so does the boundary area. Worse, the computational

complexity of DFT computational analysis increases exponentially. One alternative is to model an extra proton in the nucleus of the dangling iodide, an attempt to minimize the ionic force without increasing supercell size. This proved to be problematic in the molecule definition for QE and this direction was abandoned.

The important methylammonium cation was also created atom by atom with Avogadro, shown in Figure 3.2, along with the dipole moment. The FF model of 6 atoms and 7 bonds calculates the molecular weight of 32.065 (g/mol), Energy 1.553 (kJ/mol) and estimates the dipole moment 0.248 (D). In Figure 3.2 nitrogen is blue, carbon in gold and the 6 hydrogens in silver. The dipole moment points from the nitrogen to the carbon, as shown in the axis legend adjacent. This molecule occupies the A site of the MAPbI₃ perovskite.

Using Avogadro, the MA molecules were inserted to the A site of the two available locations maintaining the MA force field direction, as shown in Figure 3.3. This innovation causes the supercell to begin with a known structure allowing repeatability. The complete supercell framework is depicted in Figure 3.3. Figure 3.3a shows the evolving model perovskite supercell molecule with the polygon adornment. Figure 3.3b is identical to Figure 3.3a but without the polygons. This figure consists of 80 atoms with 86 bonds, with a molecular weight 9,149.563 g/mol and energy between 204.069 and 233.846 kJ/mol (depending on the orientation of the MA cation), and an estimated dipole moment between 236.500 and 148.577, depending on the orientation of the MA cation.

Even optimizing the structure using the simple FF model, several important results become evident. First, the size of the supercell is important. The larger the number of cells in the supercell, the greater the accuracy of DFT results.

Secondly, the orientation of the MA cation influences the dynamics of the properties of the material. With only the most rudimentary analysis tool of Force Field analysis, these two factors become evident. Both will play a pivotal role in quantum computational model results that follow in this chapter.

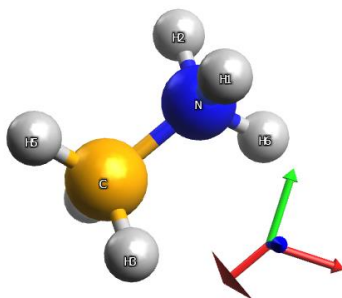


Figure 3.2 MA cation showing dipole moment and axis reference

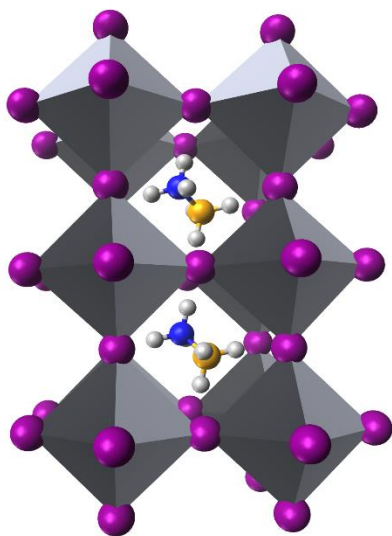


Figure 3.3a Orthorhombic MAPbI3 created atom by atom with polygons

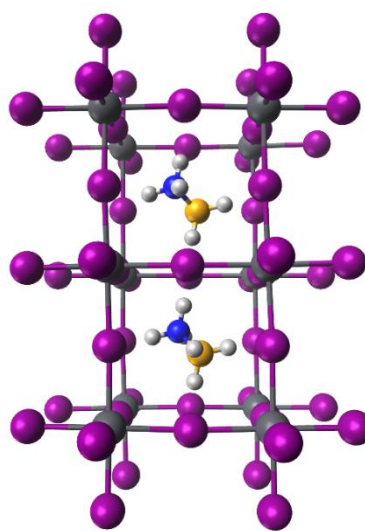


Figure 3.3b Orthorhombic MAPbI3 without polygons

3.1.1 The Unit Cell

MAPbI₃ forms an orthorhombic geometry with several space groups proposed, Pnma being common. The structure is a 3D frame consisting of four methylammonium molecules constrained in PbI₃ framework, Figure 3.4. The same unit cell is shown again in Figure 3.5 without the grey polygons and adding the iodide atoms. The latter are outside the unit cell, to complete the covalent bonds of the corner-sharing lead atoms of the unit cell. A crystal structure is a precise description of an ordered arrangement of the constituent components of a crystalline material. Ordered structures occur within a regular crystal to form a symmetric repeating group along some principal direction within the 3D material. The smallest contiguous

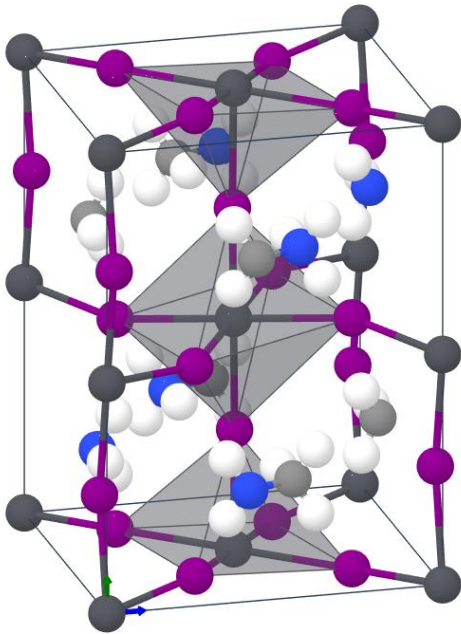


Figure 3.4 Unit cell outlined in thin black reference line, with polygons

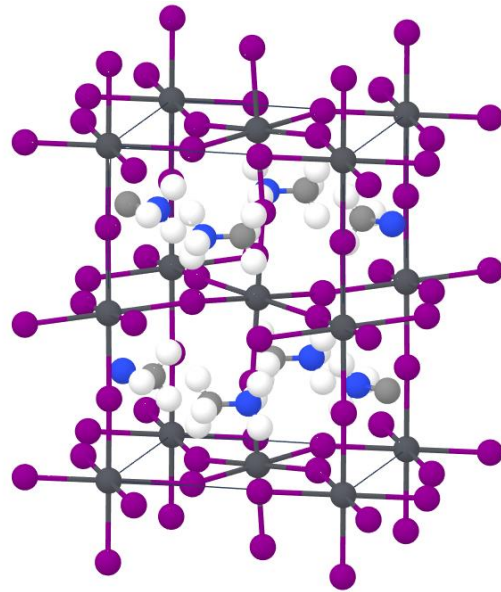


Figure 3.5 Unit cell with bonded atoms outside the Unit Cell, without polygons

group of particles that can be repeated to produce the substance is called the unit cell. The unit cell can be replicated by translation along the principal axis to produce the structure of the crystal bulk. The translations define the group of the Bravais lattice. Well behaved crystals are

characterized by a crystal family and crystal system and space group. Material such as silicon or diamond have well defined Bravais lattices with a ridged framework. These so-called hard crystals demonstrate little crystal movement and the atomic framework activity is termed lattice vibration.

By comparison to a hard-crystal, MAPbI₃ is a soft-crystal with shape shifting characteristics induced by the thermal environment and from the mobility of the MA group within the Pb-I framework. Further, the MA possesses a dipole moment. This dipole interacts with the Pb-I frame and interacts with other nearby MA groups. This dynamic environment induces stress and torques within a localized Pb-I framework complicating classifying the MAPbI₃ to a single space group.

3.1.2 Selection of the Supercell

A supercell provides a means of minimizing surface boundary model effects that are not present within the bulk. Consider the partial unit depicted in Figure 3.5. Atoms at the boundary, iodide in this case, do not represent the correct structural makeup of those within the bulk as these surface cells are disconnected from where further out units would reside. Computational analysis of this Pb centered partial unit cell renders unrealistic results. Additional elements, typically unit cells, must surround the core structure to better mimic the structure in the bulk. The larger the supercell, the more the supercell behaves like the bulk. However, the larger the supercell, the greater computation algorithm complexity, on the order of the number of particles in the supercell to the fourth power, for comprehensive Functional models of MAPbI₃.

A 3 x 3 x 3 supercell was selected as the basis for all models in this study and depicted in Figure 3.6. The tetrahedral contains the Pb atom, Iodide is shown in magenta as before, and the

MA group, H-C-N-H is shown in silver, blue, white and silver. This arrangement creates a central Pb-centered unit cell surrounded on all faces and edges by another complete unit cell. The configuration includes the 8 adjacent MA groups. This supercell arrangement reduces fringing (boundary surface) influences while allowing manageable computational runtimes. Both Figure 3.6a and 3.6b supercells reveal the slight tilting at the iodide of the Pb-I-Pb bonds as these images are generated post optimization.

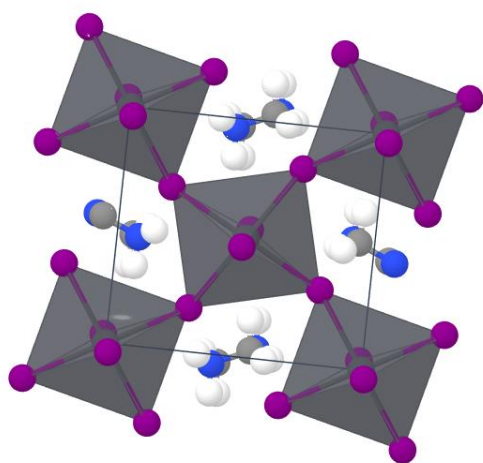


Figure 3.6a Super cell "top" view
<1,1,0>

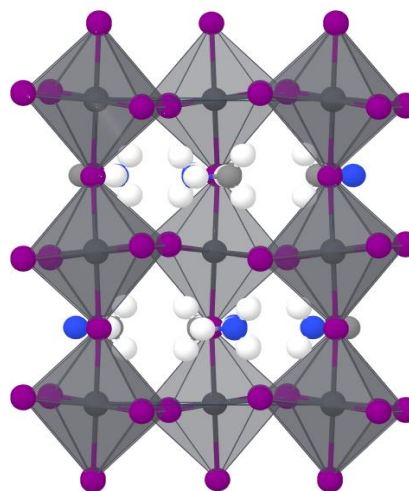


Figure 3.6b Super cell "front" view
<1,0,0>

3.2 DFT Ground-State Calculations and Results

The supercell in Figure 3.6 is the input to four representatives computational modeling methods. All computations were performed using Quantum Espresso v6.6, SSSP Efficiency PBE pseudopotential library, where smearing uses fractional occupations and K-points distance of 0.2 \AA^{-1} . For each model, the input supercell was relaxed followed by a self-consistence functional with the Kohn-Sham (K-S), or similar approximation. This is followed by the optimization Functional, iterating over the dataset searching for the particle structure that

yields the lowest energy, within a predefined tolerance. The results are post processed using various utilities to generate graphic images of the atomic structure and calculate numeric results including cell volume, band gap, energy band and Density of States diagrams.

3.2.1 Exact Exchange (HF) Hybrid PBE0

The PBE0 (Perdew–Burke–Ernzerhof) implements a Hartree-Fock hybrid DFT functional that includes the Fock exchange with a local (or semi-local) density functional. The resulting band structure, normalized to a zero Fermi level, and density of states diagrams are shown in Figure 3.7. The bandgap calculation is 1.7575 eV, density 4.013 g/cm³, total energy -204.2650 eV and volume of 1026.120 Å³.

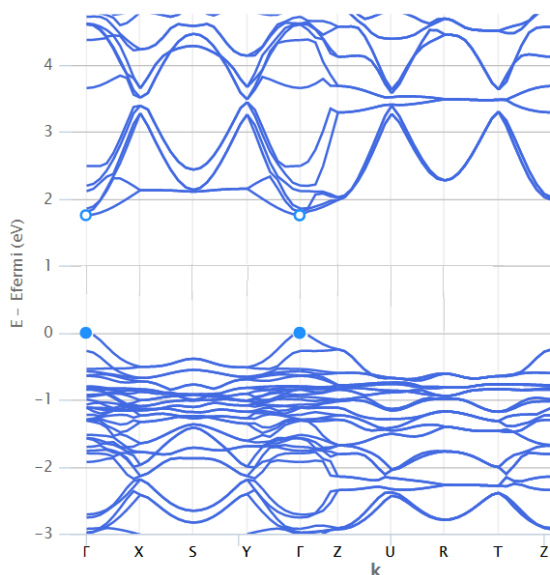


Figure 3.7a Exact exchange (HF) hybrid PBE0 band structure

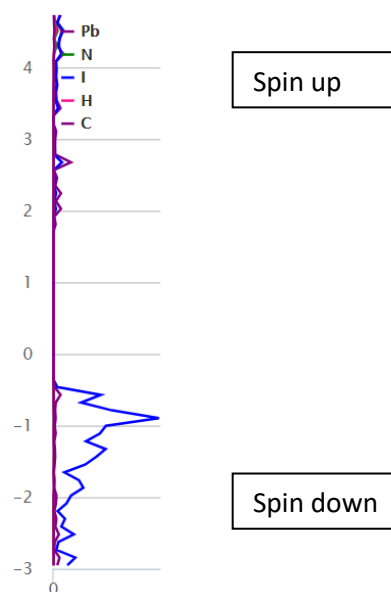


Figure 3.7b Exact exchange (HF) hybrid PBE0 band DOS

3.2.2 PAW Projector Augmented Waves with SOC

Projector Augmented Wave (PAW) is an ab initio molecular dynamic, all-electron wave Functional that constructs a fictitious Lagrangian that provides a theoretical basis for pseudopotentials and is computationally efficient. PAW unifies the all-electron and pseudopotential approaches. The theory is based on the transformation of physical wave function into auxiliary wave functions with the goal of smoothing the auxiliary wave function that can be represented in a plane wave expansion. The PAW employs frozen core approximations, the method truncates plane wave expansions (basis set), and truncates partial wave expansions (augmentation). These approximations allow good computation efficiencies and offers plane wave convergence comparable to ultrasoft pseudopotentials, in the 30 Ry range. The resulting band structure, normalized to a zero Fermi level, and density of states diagrams are shown in Figure 3.8. The bandgap calculation is 1.594 eV, density 4.019 g/cm³, total energy -204.2591 eV and volume of 1024.627 Å³.

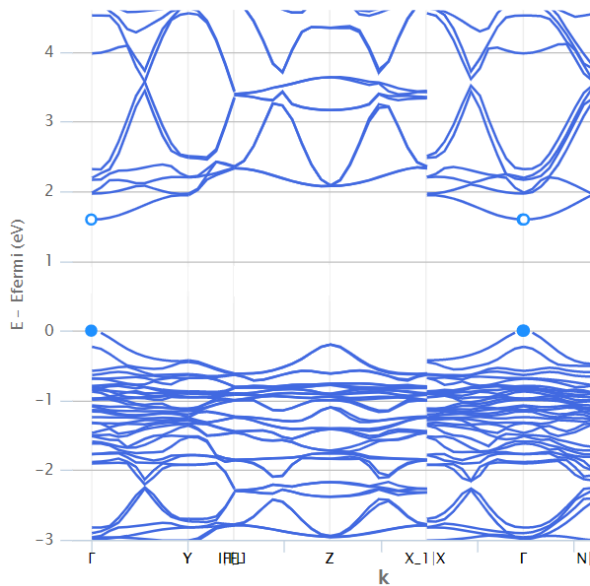


Figure 3.8a PAW with spin orbital coupling band structure

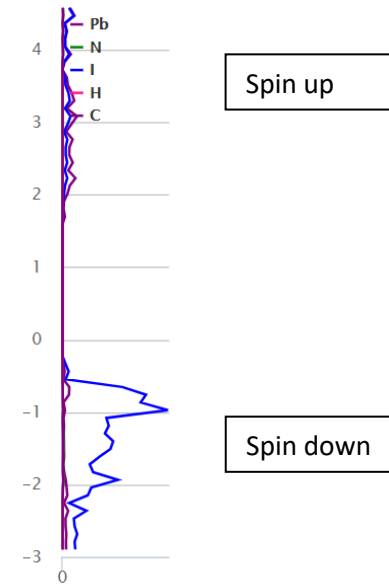


Figure 3.8b PAW with spin orbital coupling DOS

3.2.3 Generalized-gradient Approximation Model

The gradient corrected approximation method Functional depends on the local density and its gradient and is based on the uniform electron gas approximation. In condensed matter molecules, the electron density can vary greatly over small regions. An improvement to the method is to consider both the density and the gradient of the density which leads to a gradient corrected Functional, the Generalized Gradient Approximations (GGA). In this model, the approximate exchange correlation hybrid Function B3LYP (Becke three-parameter Lee-Yang-Parr) functional was used. This functional is commonly used and is considered the standard for the exchange-correlation energy calculations. There exists many other LDA type Functionals, yet this Functional is in wide use since the mid 1980's. Both DFT and Hartree-Fock methods aim to model electron correlation, yet both have drawbacks. The HF Functionals exactly model exchange correlation but with poor results recovering dynamic electron correlation. DFT models have an exact dynamic electron correlation but DFT is not quantum mechanical. Therefore it must approximate exchange correlation, which increases uncertainty and error.

The resulting band structure, normalized to a zero Fermi level, and density of states diagrams are shown in Figure 3.9. The bandgap calculation is 1.639 eV, density 3.79 g/cm³, total energy of -203.630 eV and volume of 1087.410 Å³.

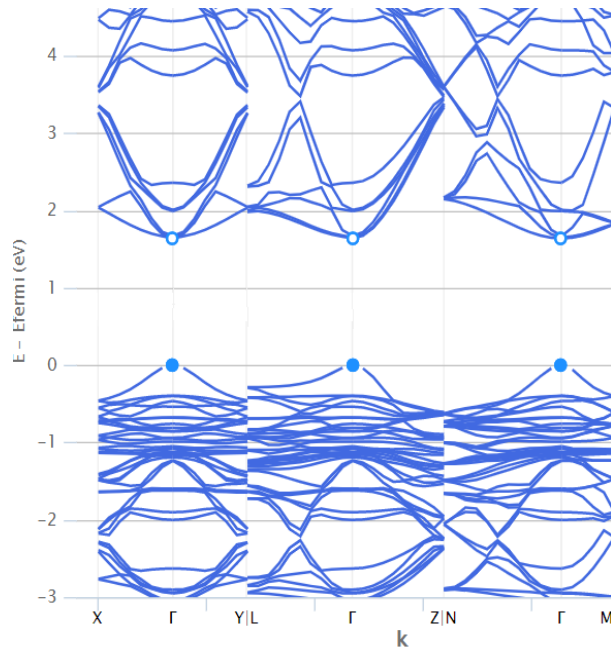


Figure 3.9a GGA corrected band structure

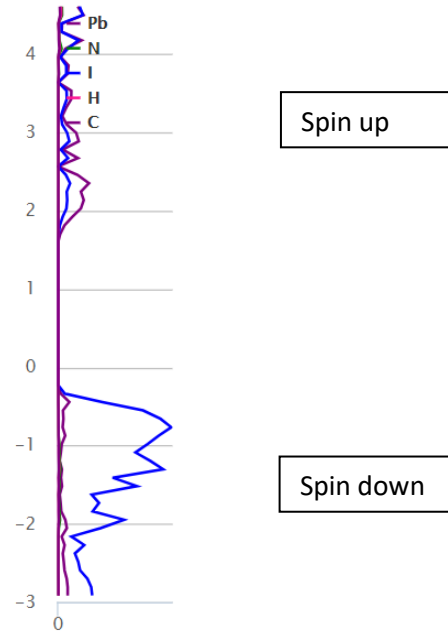


Figure 3.9b GGA corrected DOS

3.2.4 Ultrasoft (Vanderbilt) Pseudo-potentials

Ultrasoft pseudopotentials were proposed by Vanderbilt in 1980 to allow calculations for plane-wave basis sets with the lowest possible cutoff energy. The principal of pseudopotentials derives from the idea that core electrons, those electrons not in outer shells, screen the nucleus, such that only the valence electron can be considered. This allows the core to be considered a fixed charge. An advantage is a smooth potential, reducing the expansion of K-S orbitals, hence decreasing computational complexity. A prime disadvantage of lumping the nucleus and inner electrons into a core is the wavefunction in the core cannot be accurately modeled – an approximation trading accuracy for efficiency. This is concerning where electronically complex atoms, like Pb with several inner shells are near the potential of the valence electrons. This frozen core model masks the effects of interaction between electrons considered non-valence.

The resulting band structure, normalized to a zero Fermi level, and density of states diagrams are shown in Figure 3.9. The bandgap calculation is 1.639 eV, density 3.79 g/cm³, total energy of -203.630 eV and volume of 1087.410 Å³.

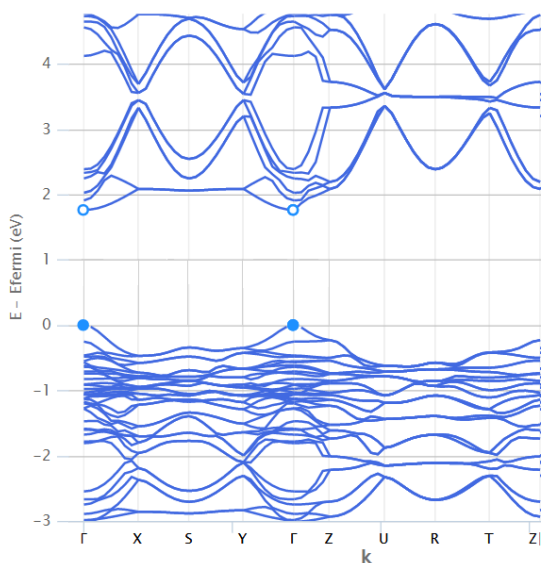


Figure 3.10a Ultrasoft pseudo-potentials band structure

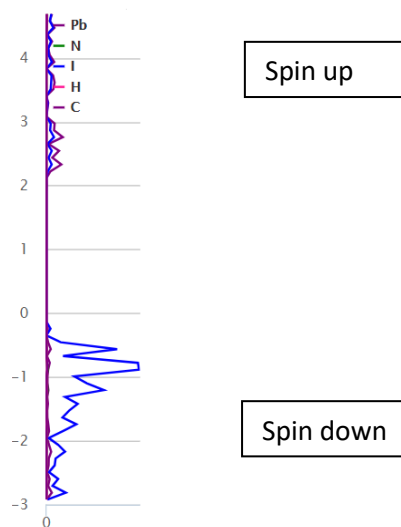


Figure 3.10b Ultrasoft pseudo-potentials DOS

3.3 Summary of Methods Results

The optimized supercell structure indicates that in the PbI₃ framework, each Pb²⁺ bonds to six I (Iodide) atoms in a corner-sharing PbI₆ octahedra. This octahedron is tilted between 12° to 29° relative to adjacent octahedra with two shorter Pb-I bond lengths of 3.248 Å, and four longer Pb-I bond lengths of 3.2601 Å, evident in Figure 3.6a in the Pb-I-Pb bond angles between the centered polygon and each outer polygon. This tilting causes two inequivalent Iodide sites. The first Iodide site is bonded in a distorted linear geometry to two equivalent Pb²⁺. The second Iodide site is bonded in a bent 151° geometry to two equivalent Pb²⁺. These measurements are taken from post processing the data and measured using Avogadro.

For MAPbI₃, methods that do not incorporate SOC calculations produce significant error in the band gap and band structure. Specifically, density based Functionals, including LDA, PEB and GGA methods produce plausible results for both band gap and energy bands while neglecting the SOC effects. However, Mosconi and Brivio et al., reported that these DFT methods, while in good agreement with experimental results, are caused by cancellation of two concurrent errors [95, 96]. This finding supports the hypothesis that SOC interactions are of significant importance to the optoelectronic properties of the material. SOC accounts for 1eV-1.1eV of the bandgap in MAPbI₃. Analysis with a SOC sensitive Functional significantly modifies band structures as shown by comparing Figures 3.7 to 3.8.

DFT models that rely upon local and semi-local Functionals, including both LDA and GGA calculations, severely underestimate the band gap. Calculated versus experimentally measured band gaps disagree by a factor of 2 [96]. These band gap discrepancies are attributed to approximations in the exchange correlation models and mathematical approximations due to mathematical function discontinuity in derivative calculations since the actual electron density is discontinuous in a quantum mechanical system.

Results from the data produced by the QE is compiled in Table 2. For comparison, Table 3 contains a list of band gaps for MAIPbI₃ published by others. Other data presented in Table 2 are not generally available. Of the methods studied, only PAW with SOC is in close agreement with experimental results.

Table 2 - Modeling optimizations final structure result summary

Method	Formation Energy / Atom eV	Density g/cm ³	Band Gap eV	Space Group	Total Energy eV	Energy per atom eV	Volume Å ³
Exact Exchange (HF) hybrid PBE0	-0.514	4.013	1.763	Pnma	- 204.2650	-4.2560	1026.120
PAW - Projector Augmented Waves w/SOC	-0.514	4.019	1.594	Cc	- 204.2591	-4.2554	1024.627
Generalized-gradient corrections GGA PBE	-0.500	3.790	1.639	P1	- 203.6300	-4.2423	1087.410
Ultrasoft (Vanderbilt) pseudo-potentials	-0.502	4.020	1.757	Pnma	- 203.7034	-4.2438	1024.208

Table 3 – Published band gap values by others

Researcher	Citation	Reported Band Gap eV
Jaing	[97]	1.5
Noh	[98]	1.5
Wang	[99]	around 1.5
Atourki	[100]	1.59

Chapter 4: Conclusions

Computational modeling is a valuable research tool in understanding the quantum mechanical interaction of electronic material. This study specifically focuses on MAIPb₃, providing methods to calculate the electronic and structural characteristics that cannot be directly measured. Selecting the proper quantum mechanical model approximations is critical to obtain accurate results.

Several widely used *ab initio*-based computation computing methods are employed to study the structural and electronic properties of a MAPbI₃ single-crystal. This research calculates the band structure and density of state using four diverse Functionals. The methods studied are Hartree-Fock based exact exchange Hybrid PBE0, the Augmented Wave (PAW), the Generalized-Gradient Approximation (GGA) and the Ultrasoft Pseudopotentials Functionals, each calculating a bandgap energy of 1.763 eV, 1.594 eV, 1.639 eV and 1.757 eV, respectively.

The Ultrasoft pseudopotential Functions frozen core model produces poor results due to the Pb non-valence (frozen) inner shell electrons interacting with other atomic valiance electrons.

Computationally efficient density-base Functionals, such as local-density approximation (LDA) and semi-local generalized gradient approximations (GGA) produce reasonable bandgap results while neglecting SOC. Yet, other research indicates these seemingly reasonable bandgap calculations are a result of opposing cancellation errors.

I interpret the data to conclude that SOC interactions are a critical factor in computing the electronic properties of MAPbI₃.

Of the methods studied, PAW, that incorporates spin-orbital coupling, calculates the most accurate results compared to experimental reports.

4.1 Future Research

The quantum mechanical modeling methods that incorporate SOC, as presented here, are comparable with experimental results reported by others. These basic models can now be extended to investigate the thermal effects of the material, the effects of including van der Waals forces, defects in the bulk, to name but a few. Questions of the electronic response varying with temperature, pressure and optical excitation can be examined. Models can be constructed to analyze the behavior of the material in an electric or magnetic field. The surface interface characteristics between perovskites and other material, including other species of perovskites, can be modeled and studied.

There remain the poorly understood effects of the free cation interaction with the metal-halogen framework. It is unclear as to the processes induced by the mobile MA cation, its effect on carrier mobility and the source of the anomalous I-V hysteresis. The charge transport of the photovoltaic properties continues to be a research topic. The process behind the reported piezo effect and its interplay with other molecular properties remains an open question. Conflicting report of the space group selection vis a vis the conductivity is debated. These, and likely many more properties can be explored with computational modeling methods.

References

1. Occhialini, C.A., et al., *Negative thermal expansion near the precipice of structural stability in open perovskites*. *Frontiers in chemistry*, 2018. **6**: p. 545.
2. Herz, L.M., *Charge-carrier mobilities in metal halide perovskites: fundamental mechanisms and limits*. *ACS Energy Letters*, 2017. **2**(7): p. 1539-1548.
3. Xu, W., et al., *Rational molecular passivation for high-performance perovskite light-emitting diodes*. *Nature Photonics*, 2019. **13**(6): p. 418-424.
4. Filippetti, A., et al., *Appealing perspectives of hybrid lead–iodide perovskites as thermoelectric materials*. *The Journal of Physical Chemistry C*, 2016. **120**(50): p. 28472-28479.
5. Spina, M., et al., *Microengineered CH₃NH₃PbI₃ Nanowire/Graphene Phototransistor for Low-Intensity Light Detection at Room Temperature*. *Small*, 2015. **11**(37): p. 4824-4828.
6. Kingon, A., et al., *High-permittivity perovskite thin films for dynamic random-access memories*. *Mrs Bulletin*, 1996. **21**(7): p. 46-52.
7. Ishihara, T., *Optical properties of Pbl-based perovskite structures*. *Journal of luminescence*, 1994. **60**: p. 269-274.
8. Cheng, Z. and J. Lin, *Layered organic–inorganic hybrid perovskites: structure, optical properties, film preparation, patterning and templating engineering*. *CrystEngComm*, 2010. **12**(10): p. 2646-2662.
9. Zhang, M., et al., *Reconfiguration of interfacial energy band structure for high-performance inverted structure perovskite solar cells*. *Nature communications*, 2019. **10**(1): p. 1-9.
10. Frova, A. and P. Boddy, *Optical field effects and band structure of some perovskite-type ferroelectrics*. *Physical Review*, 1967. **153**(2): p. 606.
11. Hussain, A.A., A.K. Rana, and M. Ranjan, *Air-stable lead-free hybrid perovskite employing self-powered photodetection with an electron/hole-conductor-free device geometry*. *Nanoscale*, 2019. **11**(3): p. 1217-1227.
12. Tanaka, K., et al., *Comparative study on the excitons in lead-halide-based perovskite-type crystals CH₃NH₃PbBr₃ CH₃NH₃PbI₃*. *Solid state communications*, 2003. **127**(9-10): p. 619-623.
13. Wang, D., et al., *Stability of perovskite solar cells*. *Solar Energy Materials and Solar Cells*, 2016. **147**: p. 255-275.
14. Berhe, T.A., et al., *Organometal halide perovskite solar cells: degradation and stability*. *Energy & Environmental Science*, 2016. **9**(2): p. 323-356.
15. Varadwaj, P.R., et al., *Significance of hydrogen bonding and other noncovalent interactions in determining octahedral tilting in the CH₃NH₃PbI₃ hybrid organic-inorganic halide perovskite solar cell semiconductor*. *Scientific reports*, 2019. **9**(1): p. 1-29.

16. El-Mellouhi, F., et al., *Hydrogen bonding and stability of hybrid organic–inorganic perovskites*. ChemSusChem, 2016. **9**(18): p. 2648-2655.
17. Unger, E.L., et al., *Hysteresis and transient behavior in current–voltage measurements of hybrid-perovskite absorber solar cells*. Energy & Environmental Science, 2014. **7**(11): p. 3690-3698.
18. Snaith, H.J., et al., *Anomalous hysteresis in perovskite solar cells*. The journal of physical chemistry letters, 2014. **5**(9): p. 1511-1515.
19. Kim, H.-S. and N.-G. Park, *Parameters affecting I–V hysteresis of CH₃NH₃PbI₃ perovskite solar cells: effects of perovskite crystal size and mesoporous TiO₂ layer*. The journal of physical chemistry letters, 2014. **5**(17): p. 2927-2934.
20. Strelcov, E., et al., *CH₃NH₃PbI₃ perovskites: Ferroelasticity revealed*. Science advances, 2017. **3**(4): p. e1602165.
21. You, Y.-M., et al., *An organic-inorganic perovskite ferroelectric with large piezoelectric response*. Science, 2017. **357**(6348): p. 306-309.
22. Leguy, A.M., et al., *Experimental and theoretical optical properties of methylammonium lead halide perovskites*. Nanoscale, 2016. **8**(12): p. 6317-6327.
23. Amat, A., et al., *Cation-induced band-gap tuning in organohalide perovskites: interplay of spin–orbit coupling and octahedra tilting*. Nano letters, 2014. **14**(6): p. 3608-3616.
24. Mitzi, D.B., *Solution-processed inorganic semiconductors*. Journal of Materials Chemistry, 2004. **14**(15): p. 2355-2365.
25. Mitzi, D.B., *Templating and structural engineering in organic–inorganic perovskites*. Journal of the Chemical Society, Dalton Transactions, 2001(1): p. 1-12.
26. Eames, C., et al., *Ionic transport in hybrid lead iodide perovskite solar cells*. Nature communications, 2015. **6**(1): p. 1-8.
27. VanLeeuwen, B.K. and V. Gopalan, *The antisymmetry of distortions*. Nat Commun, 2015. **6**: p. 8818.
28. Lee, J.-H., et al., *Resolving the Physical Origin of Octahedral Tilting in Halide Perovskites*. Chemistry of Materials, 2016. **28**(12): p. 4259-4266.
29. Wakamiya, A., et al., *Reproducible fabrication of efficient perovskite-based solar cells: X-ray crystallographic studies on the formation of CH₃NH₃PbI₃ layers*. Chemistry Letters, 2014. **43**(5): p. 711-713.
30. Supasai, T., et al., *Formation of a passivating CH₃NH₃PbI₃/PbI₂ interface during moderate heating of CH₃NH₃PbI₃ layers*. Applied Physics Letters, 2013. **103**(18): p. 183906.
31. Rajamanickam, N., et al., *Stable and durable CH₃NH₃PbI₃ perovskite solar cells at ambient conditions*. Nanotechnology, 2016. **27**(23): p. 235404.
32. Oku, T., *Crystal structures of CH₃NH₃PbI₃ and related perovskite compounds used for solar cells*. Solar Cells-New Approaches and Reviews, 2015. **1**.
33. Fu, W., et al., *Controlled crystallization of CH₃NH₃PbI₃ films for perovskite solar cells by various PbI₂ (X) complexes*. Solar Energy Materials and Solar Cells, 2016. **155**: p. 331-340.
34. Dong, Q., et al., *Electron-hole diffusion lengths > 175 μm in solution-grown CH₃NH₃PbI₃ single crystals*. Science, 2015. **347**(6225): p. 967-970.

35. Zu, F., et al., *Constructing the Electronic Structure of CH₃NH₃PbI₃ and CH₃NH₃PbBr₃ Perovskite Thin Films from Single-Crystal Band Structure Measurements*. The journal of physical chemistry letters, 2019. **10**(3): p. 601-609.
36. Ziffer, M.E., J.C. Mohammed, and D.S. Ginger, *Electroabsorption spectroscopy measurements of the exciton binding energy, electron–hole reduced effective mass, and band gap in the perovskite CH₃NH₃PbI₃*. Acs Photonics, 2016. **3**(6): p. 1060-1068.
37. Zhu, X., et al., *Computed and experimental absorption spectra of the perovskite CH₃NH₃PbI₃*. The journal of physical chemistry letters, 2014. **5**(17): p. 3061-3065.
38. Yin, W.-J., T. Shi, and Y. Yan, *Unusual defect physics in CH₃NH₃PbI₃ perovskite solar cell absorber*. Applied Physics Letters, 2014. **104**(6): p. 063903.
39. Huang, W., et al., *Observation of unusual optical band structure of CH₃NH₃PbI₃ perovskite single crystal*. ACS Photonics, 2018. **5**(4): p. 1583-1590.
40. Chae, J., et al., *Chloride Incorporation Process in CH₃NH₃PbI₃–x Cl x Perovskites via Nanoscale Bandgap Maps*. Nano letters, 2015. **15**(12): p. 8114-8121.
41. Zhou, Y., et al. *Preparation and characterization of high-quality perovskite CH₃NH₃PbX₃ (I, Br) single crystal*. in *IOP Conference Series: Materials Science and Engineering*. 2017. IOP Publishing.
42. Khorramshahi, F. and A. Takshi. *Novel fabrication of flexible perovskite photosensor using capillary motion*. in *Organic and Hybrid Sensors and Bioelectronics XI*. 2018. International Society for Optics and Photonics.
43. Pammi, S., et al., *Predominant stable MAPbI₃ films deposited via chemical vapor deposition: stability studies in illuminated and darkened states coupled with temperature under an open-air atmosphere*. ACS Applied Energy Materials, 2018. **1**(7): p. 3301-3312.
44. Jella, V., et al., *Enhanced output performance of a flexible piezoelectric energy harvester based on stable MAPbI₃-PVDF composite films*. Nano Energy, 2018. **53**: p. 46-56.
45. Gupta, R., et al., *Room Temperature Synthesis of Perovskite (MAPbI₃) Single Crystal by Antisolvent Assisted Inverse Temperature Crystallization Method*. Journal of Crystal Growth, 2020: p. 125598.
46. Ding, J., et al., *The role of surface defects in photoluminescence and decay dynamics of high-quality perovskite MAPbI₃ single crystals*. The journal of physical chemistry letters, 2018. **9**(15): p. 4221-4226.
47. Battula, R.K., et al., *Stability of MAPbI₃ perovskite grown on planar and mesoporous electron-selective contact by inverse temperature crystallization*. RSC Advances, 2020. **10**(51): p. 30767-30775.
48. MØLLER, C.K., *Crystal structure and photoconductivity of caesium plumbohalides*. Nature, 1958. **182**(4647): p. 1436-1436.
49. Dowker, H. and J.J. Halliwell, *Quantum mechanics of history: The decoherence functional in quantum mechanics*. Physical Review D, 1992. **46**(4): p. 1580.
50. Rovelli, C. and L. Smolin, *Loop space representation of quantum general relativity*. Nuclear Physics B, 1990. **331**(1): p. 80-152.
51. Maitra, N.T., et al., *Density-potential mapping in time-dependent density-functional theory*. Physical Review A, 2010. **81**(4): p. 042525.

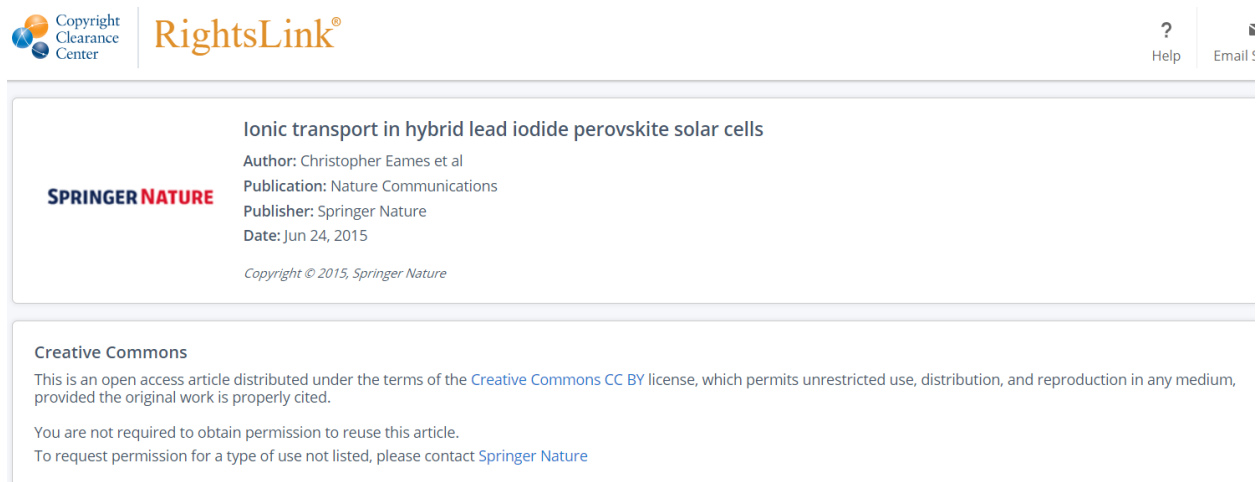
52. Chen, M., et al., *Introducing PROFESS 3.0: An advanced program for orbital-free density functional theory molecular dynamics simulations*. *Comput. Phys. Commun.*, 2015. **190**: p. 228-230.
53. Zhen-min, Z., *On quantum chemical ab initio method and precision evaluation of the calculation results by Gaussian98 program*. *原子核物理评论*, 2006. **23**(3): p. 331-334.
54. Giannozzi, P., et al., *QUANTUM ESPRESSO: a modular and open-source software project for quantum simulations of materials*. *Journal of physics: Condensed matter*, 2009. **21**(39): p. 395502.
55. Cai, Y., et al., *Computational study of halide perovskite-derived A₂BX₆ inorganic compounds: chemical trends in electronic structure and structural stability*. *Chemistry of Materials*, 2017. **29**(18): p. 7740-7749.
56. Brodersen, S., et al., *A study of different approaches to the electrostatic interaction in force field methods for organic crystals*. *Physical Chemistry Chemical Physics*, 2003. **5**(21): p. 4923-4931.
57. Allinger, N., *Calculation of molecular structure and energy by force-field methods*, in *Advances in physical organic chemistry*. 1976, Elsevier. p. 1-82.
58. Chen, J., W. Im, and C.L. Brooks, *Balancing solvation and intramolecular interactions: toward a consistent generalized Born force field*. *Journal of the American Chemical Society*, 2006. **128**(11): p. 3728-3736.
59. Hanwell, M.D., et al., *Avogadro: an advanced semantic chemical editor, visualization, and analysis platform*. *Journal of cheminformatics*, 2012. **4**(1): p. 17.
60. Visscher, K.M. and D.P. Geerke, *Deriving force-field parameters from first principles using a polarizable and higher order dispersion model*. *Journal of chemical theory and computation*, 2019. **15**(3): p. 1875-1883.
61. Griffiths, D.J. and D.F. Schroeter, *Introduction to quantum mechanics*. 2018: Cambridge University Press.
62. Magri, F., *A simple model of the integrable Hamiltonian equation*. *Journal of Mathematical Physics*, 1978. **19**(5): p. 1156-1162.
63. Koskinen, M., M. Manninen, and S. Reimann, *Hund's rules and spin density waves in quantum dots*. *Physical review letters*, 1997. **79**(7): p. 1389.
64. Simon, B., *Quantum mechanics for Hamiltonians defined as quadratic forms*. Vol. 68. 2015: Princeton University Press.
65. Miller Jr, S.C. and R. Good Jr, *A WKB-type approximation to the Schrödinger equation*. *Physical Review*, 1953. **91**(1): p. 174.
66. Strocchi, F., *The physical principles of quantum mechanics. A critical review*. *The European Physical Journal Plus*, 2012. **127**(1): p. 12.
67. Le Bellac, M., *Quantum Physics Cambridge University Press*. 2006, Cambridge.
68. Griffiths, R.B., *Consistent quantum theory*. 2003: Cambridge University Press.
69. Blöchl, P.E., *Projector augmented-wave method*. *Physical review B*, 1994. **50**(24): p. 17953.
70. Combes, J.-M., P. Duclos, and R. Seiler, *The born-oppenheimer approximation, in Rigorous atomic and molecular physics*. 1981, Springer. p. 185-213.

71. Monkhorst, H.J., *Chemical physics without the Born-Oppenheimer approximation: The molecular coupled-cluster method*. Physical Review A, 1987. **36**(4): p. 1544.
72. Dalgarno, A. and G. Victor, *The time-dependent coupled Hartree-Fock approximation*. Proceedings of the Royal Society of London. Series A. Mathematical and Physical Sciences, 1966. **291**(1425): p. 291-295.
73. Atkins, P.W. and R.S. Friedman, *Molecular quantum mechanics*. 2011: Oxford university press.
74. Booth, G.H., A.J. Thom, and A. Alavi, *Fermion Monte Carlo without fixed nodes: A game of life, death, and annihilation in Slater determinant space*. The Journal of chemical physics, 2009. **131**(5): p. 054106.
75. Assfeld, X. and J.-L. Rivail, *Quantum chemical computations on parts of large molecules: the ab initio local self consistent field method*. Chemical physics letters, 1996. **263**(1-2): p. 100-106.
76. Werner, H.-J., F.R. Manby, and P.J. Knowles, *Fast linear scaling second-order Møller-Plesset perturbation theory (MP2) using local and density fitting approximations*. The Journal of chemical physics, 2003. **118**(18): p. 8149-8160.
77. Kolorenč, J., S. Hu, and L. Mitas, *Wave functions for quantum Monte Carlo calculations in solids: Orbitals from density functional theory with hybrid exchange-correlation functionals*. Physical Review B, 2010. **82**(11): p. 115108.
78. Gunnarsson, O. and R. Jones, *Total-energy differences: Sources of error in local-density approximations*. Physical Review B, 1985. **31**(12): p. 7588.
79. Froyen, S. and W.A. Harrison, *Elementary prediction of linear combination of atomic orbitals matrix elements*. Physical Review B, 1979. **20**(6): p. 2420.
80. Simmons, J., et al., *Generalization of the basis functions of the LCAO method for band-structure calculations*. Journal of Physics C: Solid State Physics, 1975. **8**(10): p. 1549.
81. Provorse, M.R. and C.M. Isborn, *Electron dynamics with real-time time-dependent density functional theory*. International Journal of Quantum Chemistry, 2016. **116**(10): p. 739-749.
82. Bouzid, A., et al., *Role of the van der Waals interactions and impact of the exchange-correlation functional in determining the structure of glassy GeTe 4*. Physical Review B, 2015. **92**(13): p. 134208.
83. Bagayoko, D., *Understanding density functional theory (DFT) and completing it in practice*. AIP Advances, 2014. **4**(12): p. 127104.
84. Dreizler, R.M. and E.K. Gross, *Density functional theory: an approach to the quantum many-body problem*. 2012: Springer Science & Business Media.
85. Kalinin, K.P. and N.G. Berloff, *Global optimization of spin Hamiltonians with gain-dissipative systems*. Scientific reports, 2018. **8**(1): p. 1-9.
86. Sun, J., et al., *Self-consistent meta-generalized gradient approximation within the projector-augmented-wave method*. Physical Review B, 2011. **84**(3): p. 035117.
87. Proynov, E.I. and D.R. Salahub, *Simple but efficient correlation functional from a model pair-correlation function*. Physical Review B, 1994. **49**(12): p. 7874.
88. Stroppa, A. and G. Kresse, *The shortcomings of semi-local and hybrid functionals: what we can learn from surface science studies*. New Journal of Physics, 2008. **10**(6): p. 063020.

89. Kossmann, S., B. Kirchner, and F. Neese, *Performance of modern density functional theory for the prediction of hyperfine structure: meta-GGA and double hybrid functionals*. *Molecular Physics*, 2007. **105**(15-16): p. 2049-2071.
90. Hellmann, H., *A new approximation method in the problem of many electrons*. *The Journal of Chemical Physics*, 1935. **3**(1): p. 61-61.
91. Smallwood, C.J., et al., *A computationally efficient exact pseudopotential method. I. Analytic reformulation of the Phillips-Kleinman theory*. *The Journal of chemical physics*, 2006. **125**(7): p. 074102.
92. McEachran, R.P., C. Tull, and M. Cohen, *Frozen core approximation for atoms and atomic ions*. *Canadian Journal of Physics*, 1968. **46**(23): p. 2675-2678.
93. This work has been released into the public domain by its author, Wquester at English Wikipedia. This applies worldwide.
94. Fuchs, M. and M. Scheffler, *Ab initio pseudopotentials for electronic structure calculations of poly-atomic systems using density-functional theory*. *Computer Physics Communications*, 1999. **119**(1): p. 67-98.
95. Brivio, F., et al., *Relativistic quasiparticle self-consistent electronic structure of hybrid halide perovskite photovoltaic absorbers*. *Physical Review B*, 2014. **89**(15): p. 155204.
96. Mosconi, E., et al., *First-principles modeling of mixed halide organometal perovskites for photovoltaic applications*. *The Journal of Physical Chemistry C*, 2013. **117**(27): p. 13902-13913.
97. Jiang, S., et al., *Pressure-Dependent Polymorphism and Band-Gap Tuning of Methylammonium Lead Iodide Perovskite*. *Angewandte Chemie*, 2016. **128**(22): p. 6650-6654.
98. Noh, J.H., et al., *Chemical management for colorful, efficient, and stable inorganic-organic hybrid nanostructured solar cells*. *Nano letters*, 2013. **13**(4): p. 1764-1769.
99. Wang, B., X. Xiao, and T. Chen, *Perovskite photovoltaics: a high-efficiency newcomer to the solar cell family*. *Nanoscale*, 2014. **6**(21): p. 12287-12297.
100. Atourki, L., et al., *Role of the chemical substitution on the structural and luminescence properties of the mixed halide perovskite thin MAPbI₃- xBr_x (0 ≤ x ≤ 1) films*. *Applied Surface Science*, 2016. **371**: p. 112-117.

Appendix A: Copyright Permissions

1) The permission below is for the use of Figure 1.1:



The screenshot shows the top of a Springer Nature article page. On the left, there are logos for the Copyright Clearance Center and RightsLink. On the right, there are links for Help and Email. The main content area displays the article title "Ionic transport in hybrid lead iodide perovskite solar cells", the author "Christopher Eames et al", the publication "Nature Communications", the publisher "Springer Nature", and the date "Jun 24, 2015". Below this, it states "Copyright © 2015, Springer Nature". A Creative Commons section follows, stating that the article is distributed under the CC BY license, which allows unrestricted use, distribution, and reproduction in any medium, provided the original work is properly cited. It also notes that permission is not required to reuse the article and provides a link to contact Springer Nature for other types of permission.

2) The permission below is for the use of Figure 1.2:


Image from: “Negative Thermal Expansion Near the Precipice of Structural Stability in Open Perovskites”. Ref: <https://www.frontiersin.org/articles/10.3389/fchem.2018.00545/full>

Copyright © 2018 Occhialini, Guzmán-Verri, Handunkanda and Hancock. This is an open-access article distributed under the terms of the **Creative Commons Attribution License (CC BY)**. The use, distribution or reproduction in other forums is permitted, provided the original author(s) and the copyright owner(s) are credited and that the original publication in this journal is cited, in accordance with accepted academic practice. No use, distribution or reproduction is permitted which does not comply with these terms.


3) The permission below is for the use of Figure 2.1:

Pseudopotential and pseudo-wavefunction comparison. r_c is the cutoff radius where the two correlate and is 1 adapted from “Sketch Pseudopotentials” by Wolfram Qeuster. Original uploader was Wqeuster at en.wikipedia—Transferred from en.wikipedia; transferred to Commons by User:Leyo using CommonsHelper. self-made with inkscape. Licensed under Public Domain via Wikimedia Commons].

Ref: https://commons.wikimedia.org/wiki/File:Sketch_Pseudopotentials.png

Description	English: Comparison of a wavefunction in the Coulomb potential of the nucleus (blue) to the one in the pseudopotential (red). The real and the pseudo wavefunction and potentials match above a certain cutoff radius r_c . Deutsch: Vergleich einer Wellenfunktion im Coulomb Potential des Nucleus (blau) mit einer im Pseudopotential (rot). Die echte und die Pseudo-Wellenfunktion und die Potentiale selbst stimmen oberhalb des cutoff Radius r_c überein.
Date	22 November 2006 (original upload date)
Source	Own work  This PNG graphic was created with Inkscape .
Author	Wolfram Qvester

Licensing [\[edit \]](#)



This work has been released into the **public domain** by its author, **Wqvester at English Wikipedia**. This applies worldwide.

In some countries this may not be legally possible; if so:
*Wqvester grants anyone the right to use this work **for any purpose**, without any conditions, unless such conditions are required by law.*

4) The permission below is for the use of Figure B.1

Figure B.1 is an excerpt from: “NREL Best Research-Cell Efficiencies as of 08/03/2020”.

Source: <https://www.nrel.gov/pv/cell-efficiency.html>, a U.S. Government Agency, therefore not restricted use.

Appendix B: NREL Best Research-Cell Efficiencies as of 08/03/2020

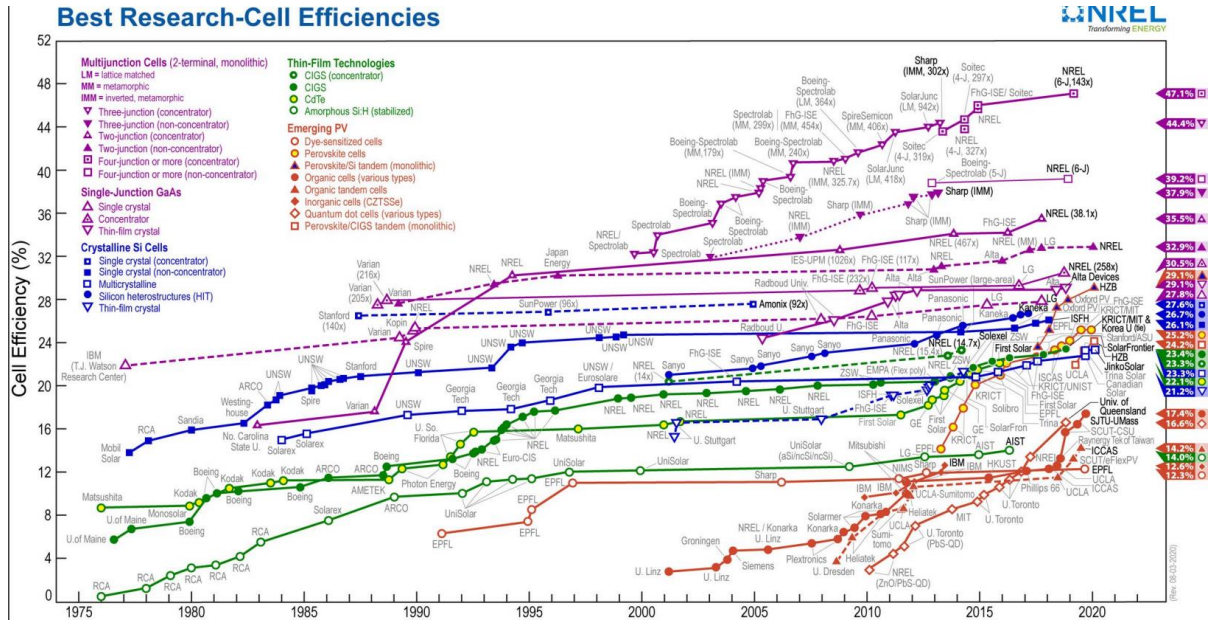


Figure B.1 NREL Best Research-Cell Efficiencies as of 08/03/2020

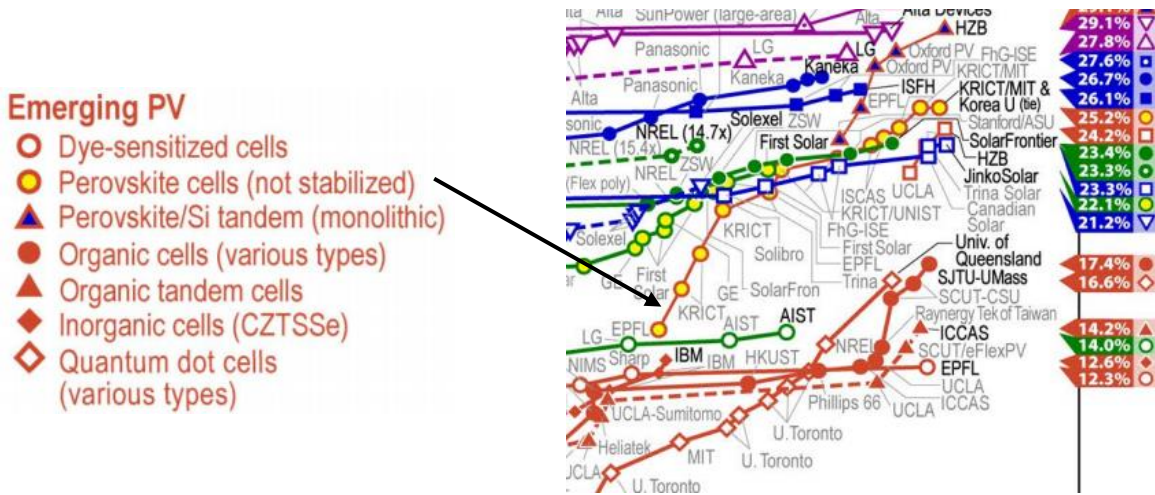


Figure B.1a Perovskites inset of NREL Best Research-Cell Efficiencies as of 08/03/2020. Courtesy of the National Renewable Energy Laboratory, Golden, Colorado.